Particle diffraction studied using quantum trajectories

A S Sanz[1], F Borondo[1] and S Miret-Artés[2]

[1] Departamento de Química, C-IX, Universidad Autónoma de Madrid, Cantoblanco-28049, Madrid, Spain
[2] Instituto de Matemáticas y Física Fundamental, Consejo Superior de Investigaciones Científicas, Serrano 123, 28006 Madrid, Spain

E-mail: angel.sanz@uam.es, f.borondo@uam.es and salvador@fam10.imaff.csic.es

Abstract
Diffraction and interference of matter waves are key phenomena in quantum mechanics. Here we present some results on particle diffraction in a wide variety of situations, ranging from simple slit experiments to more complicated cases such as atom scattering by corrugated metal surfaces and metal surfaces with simple and isolated adsorbates. The principal novelty of our study is the use of the so-called Bohmian formalism of quantum trajectories. These trajectories are able to satisfactorily reproduce the main features of the experimental results and, more importantly, they provide a causal intuitive interpretation of the underlying dynamics. In particular, we will focus our attention on: (a) a revision of the concepts of near and far field in undulatory optics; (b) the transition to the classical limit, where it is found that although the quantum and classical diffraction patterns tend to be quite similar, some quantum features are maintained even when the quantum potential goes to zero; and (c) a qualitative description of the scattering of atoms by metal surfaces in the presence of a single adsorbate.

Contents

1. Introduction

Quantum mechanics is a general theory that satisfactorily explains a wide variety of phenomena ranging from atomic and subatomic scales to the macroscopic level. Diffraction, which is characteristic of the undulatory motion, is at the core of quantum mechanics, together with discreteness and coherence [1]. The importance of these phenomena at the quantum level is obvious, for example, in the Schrödinger representation of quantum mechanics which is called, accordingly, wave mechanics and is governed by a linear wave equation. In this sense, the introduction of the quantum behaviour given by Feynman in his famous *Lectures on Physics* [2] is paradigmatic.

From the early diffraction experiment by Davisson and Germer in 1927, confirming de Broglie's conjecture on the undulatory nature of electrons, the technology involved has been improving day by day and many other experiments have been performed with different kinds of probe particle, such as neutrons [3,4]. Very recently, a series of very interesting diffraction experiments with heavy particles, such as van der Waals clusters and fullerenes, has also been reported in the literature [5,6].

In surface scattering, diffraction experiments are also of paramount importance [7–9]. Low-energy incident beams of light neutral particles are able to probe, in a non-destructive fashion, the outermost layer of metallic, insulator, and semiconductor surfaces. In particular, experiments with helium atoms have been widely carried out and, due to the small value of the mass, the scattering is predominantly elastic and diffraction effects dominate. This has led to the obtaining of a wealth of data and a lot of information about, for example, the orientation and size of the surface unit cells, surface corrugations, particle–surface physisorption potentials, surface diffusion, condensation, and growth phenomena. Inelastic processes can also be studied and phonon dispersion curves are determined by combining pulsed beams and time-of-flight techniques [10,11]. The thermal vibrations of the surface (even those corresponding to the zero-point motion) can induce inelastic scattering of the incoming atoms, leading to an attenuation of the diffraction intensities without changing their shapes. This is a well-known phenomenon in neutron and x-ray diffraction, where the Debye–Waller (exponential) factor is used to account for this effect. Furthermore, if heavier probe particles are used, the corresponding scattering enhances the relevance of multiphoton processes. Trapping and subsequent desorption [12,13] can be assisted by inelastic events. Here, different mechanisms compete and/or cooperate in the desorption, which makes the process very interesting from a dynamical point of view. The possibility of using molecules as scattering particles is also very interesting since the internal (rotational and vibrational) degrees of freedom also enter into play. Finally, sticking of particles [14] and chemical reactions may also take place [15].

A rigorous treatment of atom–surface scattering must be quantum mechanical, and different close-coupling methods have been developed, ranging from the early one due to

Wolken [16] to more sophisticated ones such as that based on the Kohn principle [17] and the so-called phonon dressing formalism [18]. However, it is well established [19] that a classical approach is an excellent approximation in many cases. For example, the rainbow scattering where a static potential can be used to describe it [20]. In this way, McClure [21] was able to satisfactorily reproduce the available experimental data concerning surface rainbows, and many other classical studies have been reported in the literature [22]. The main advantage of the classical approach is that it provides a tremendous insight into the physical processes studied. In particular, it has been conjectured [23, 24] that the temporary trapping of some particles by the attractive well in the vicinity of the surface lies at the origin of the so-called selective adsorption resonances [25] occurring, for example, in the scattering of He atoms by corrugated Cu surfaces [26]. However, when the corresponding classical trajectories were studied in more detail [27], it was shown to be a nice illustration of chaotic scattering [28] (sensitivity to initial conditions). The resulting trapping could not be thought to be the only physical mechanism explaining the selective adsorption [29].

On the other hand, when the incident atom is light, quantum mechanical effects [30] (such as diffraction) are too important and then semiclassical theories are needed to properly treat the problem [31]. Among them, the application of the classical S-matrix theory [23, 32] deserves special mention. These semiclassical improvements to the pure classical analysis are able to significantly extend the range of systems in which theory and experiment satisfactorily agree.

A theoretical formalism combining both the accuracy of the predictions of quantum mechanics and the capability of providing an intuitive interpretation of the physical phenomena involved (analogous to that of the classical description in which individual aspects of material particles are fully described) is the quantum theory of motion developed by Bohm [33]. This alternative formalism of quantum mechanics, similarly to Madelung's 'hydrodynamical' formulation of quantum mechanics [34], introduces a polar form for the wavefunction into the Schrödinger equation, and the de Broglie concept of the pilot wave [35]. In this way Bohm [36] developed a formalism in which the initial and final states of a process are causally connected by quantum trajectories, presenting significant conceptual differences from the conventional Copenhagen interpretation [37]. The quantum potential appearing in this theory provides a different and clear insight into quantum interference, without the need to abandon the notion of well-defined trajectories. Particles are guided by a surrounding wave, a solution of the Schrödinger equation, such that the spacetime orbits of an ensemble of particles reproduce the statistical quantum predictions.

In addition to its interpretative importance [38], there has recently been renewed interest in the de Broglie–Bohm (BB) theory from the computational point of view. For example, Hirschfelder *et al* [39] and Dewdney and Hiley [40] studied the scattering by a square barrier, Philippidis *et al* [41] considered the diffraction through two slits, Dewdney *et al* [42] explained spin superposition, spin measurements, and Einstein–Podolsky–Rosen spin correlations in terms of individual particle trajectories (with continuously variable spin vectors), and Brown *et al* [43] considered the problem of identical particles within the BB formalism. Parmenter and Valentine [44], and Konkel and Makowski [45] have studied chaos in Bohmian trajectories, showing examples where they diverge exponentially. Furthermore, quantum wavepacket propagation schemes in the gas phase and based on quantum trajectories have also been developed [46–48]. In the atom–surface scattering context, Sanz *et al* have applied the BB formalism to reinterpret diffraction patterns [49] and the rainbow effect [50] has been analysed from the quantum trajectories point of view. Finally, a mixed quantum/classical mechanics method based also on Bohmian trajectories has been successfully applied to a different problem in the gas phase [51] as well as in surface scattering [52].

In this article we present a short review of the application of the BB theory to diffraction, giving several examples of diffraction by slits that have been measured in the recent past, as well as atom–surface scattering experiments. Special attention will be paid to the description of the implied numerical methods and some of the most relevant results will be reported and discussed.

2. The causal interpretation of quantum mechanics

Since the beginning of quantum mechanics, this theory introduced in physics the polemical problem of the interpretation of measurement [53] which still remains an open question. Moreover, uncertainty has also been postulated as an intrinsic feature in quantum systems, something that should be regarded more as an old historical problem than a true experimental result. In standard quantum mechanics, it is only possible to obtain statistical results about macro-observations (carried out on unspecified and unspecifiable systems); one is forbidden to think about microscopic processes considered as individual events composed of causally connected sequences in space and time. This widely accepted way of proceeding is mirrored by the statistical interpretation of the wavefunction given by Born [54]. Thus, whereas classical systems can be studied both individually and statistically, depending on the number of particles, quantum systems only allow a statistical description, even for one single particle.

This fundamental difference between classical and quantum mechanics is clearly illustrated in experiments in which there exist two well-distinguished processes [1], such as the double-slit experiment which '*has in it the heart of quantum mechanics*' [2]. Here the first process is constituted by the preparation of particles which are directed towards a double slit and detected on a screen sufficiently far away, after passing through them; and the second process is the measurement of the arrival position on the screen. By repeating the experiment with many identical particles, one observes that the arrival position is different for each one of these particles. This implies that identical events resulting from identical preparations are not reproducible, although the source of this non-reproducibility (intrinsic indeterminism or limitations in the preparation procedure) is irrelevant for our purpose here. The final results (the patterns over the screen) are quite different for classical and quantum particles. In the classical case two well-defined probability maxima, corresponding to the two slits, are observed; they can be explained by using two probability distributions. In the quantum case the probability appears as an oscillatory function, which can be explained as the interference of two waves. According to standard quantum mechanics, the interference pattern observed appears even when the experiment is performed in conditions such that on average only one particle at a given time arrives at the screen. This explanation, coming from optical physics in which waves interfere with themselves, is commonly referred to as self-interference [7]. In the new quantum scheme, the observed pattern is considered basically granular: particles pass through one of the two slits but the total wavefunction is extended to both.

2.1. The wavefunction and equations of motion

With respect to the preceding discussion, it should be pointed out that the statistical interpretation, despite its success, is by no means forced on us by the experimental evidence. Indeed the wavefunction contains more information than mere probabilities, and it seems sensible to try to obtain from it information about causally connected individual events, from which the probabilistic properties can be easily ascertained. This is the philosophy enclosed in de Broglie's hypothesis [35], which was developed into a physical theory by Bohm in 1952 [36]. Let us define a quantum mechanical system as constituted essentially by a particle having a

precise defined position, varying continuously as a function of time, and a wave expanding in space and time, and guiding the motion of the particle. In this way, the key element in the theory is the introduction of the concept of particle, in the classical sense of following tracks in space and time, into a quantal description.

To obtain the equations of motion for such a particle, the quantum wavefunction is written in polar form:

$$\Psi(r, t) = R(r, t)e^{iS(r,t)/\hbar}, \tag{1}$$

where the real functions $R^2 = \Psi^*\Psi$ and $S = (\hbar/2i)(\ln \Psi - \ln \Psi^*)$ are the amplitude and phase of Ψ, respectively. These functions are more slowly varying than the generally oscillatory real and imaginary parts of Ψ. When the wavefunction is introduced into the time-dependent Schrödinger equation,

$$i\hbar\frac{\partial \Psi}{\partial t} = \left[-\frac{\hbar^2}{2m}\nabla^2 + V\right]\Psi, \tag{2}$$

where $V(r, t)$ is the potential due to the external classical field, two real coupled equations,

$$\frac{\partial R^2}{\partial t} + \nabla \cdot \left(R^2\frac{\nabla S}{m}\right) = 0, \tag{3}$$

$$\frac{\partial S}{\partial t} + \frac{(\nabla S)^2}{2m} + V - \frac{\hbar^2}{2m}\frac{\nabla^2 R}{R} = 0, \tag{4}$$

corresponding to the imaginary and real parts respectively, are obtained.

Given the form presented by equation (4), it is common to use a Hamilton–Jacobi type of formalism in the BB theory. As will be shown below, this formalism provides a general theory of waves and rays which goes beyond classical mechanics. Equations (3) and (4) can be interpreted, respectively, as the conservation of probability density [55], and a quantum Hamilton–Jacobi equation, similar to its classical counterpart except for an extra term:

$$Q = -\frac{\hbar^2}{2m}\frac{\nabla^2 R}{R}. \tag{5}$$

This function is called the *quantum potential* and it is due to internal quantum forces. As can be seen, it is determined by the curvature of the wavefunction amplitude. The role of Q as a potential—similar to V but of quantum origin—is more clearly seen if we rearrange equation (4) by defining a velocity field v (as is done in the classical Hamilton–Jacobi theory) as

$$v = \dot{r} = \frac{\nabla S}{m}. \tag{6}$$

This expression implies that each particle trajectory is orthogonal to the $S = $ constant manifold. By applying the operator ∇ to equation (4) and substituting (6) in the resulting expression, one obtains

$$m\frac{\partial v}{\partial t} + m(v \cdot \nabla)v = -\nabla(Q + V), \tag{7}$$

from which a generalized Newton's second law

$$m\frac{dv}{dt} = -\nabla(Q + V). \tag{8}$$

can be obtained by using the Lagrangian time derivative operator

$$\frac{d}{dt} = \frac{\partial}{\partial t} + v \cdot \nabla. \tag{9}$$

In (8) it is observed that a quantum force, $-\nabla Q$ (depending on the wavefunction), acts on the particle, in addition to the classical force given by $-\nabla V$, and then effects other than those derived from the classical potential, V, are expected.

2.2. The quantum potential

Although Bohm's theory may seem a step backwards to classical theories, this is not so since Q produces non-classical effects. For example, and as will be discussed in detail in section 4.4, V vanishes much (some orders of magnitude) earlier than Q does, and then some effects, namely those leading to diffraction in the Fraunhofer region, happen well beyond the region of action of classical forces. Moreover, and unlike classical potentials, Q is not a preassigned function of the spatial coordinates (and eventually depending also on the time), but is generally a more complicated function depending on the quantum state. That is, the introduction of a quantum potential implies a more general concept of potential than that given in classical mechanics. Due to this dependence on the quantum state, the quantum potential encodes at each point information on the whole problem exhibiting therefore a context dependence or wholeness, which implies a sensitive dependence on each parameter necessary for the description of the quantum system. The non-separability or context dependence was for a long time regarded as a fatal defect of Bohm's theory, but as Bell's theorem [56] proved, this is an inherent feature of the structure of quantum mechanics. Furthermore, given a physical problem—that is, fixing an external classical potential, V—an infinite set of different forms can be obtained for the quantum potential by means of the superposition principle for the solutions of the time-dependent Schrödinger equation, and so a corresponding set of different motions. Thus, if $\psi_k = r_k e^{is_k/\hbar}$ is one such solution of the time-dependent Schrödinger equation, the amplitude and phase of the wavefunction $\Psi = R e^{iS/\hbar}$, which is a linear combination of N of those solutions, can then be expressed as

$$R^2 = \sum_{k,l=1}^{N} r_k r_l \cos[(s_k - s_l)/\hbar], \tag{10}$$

$$\tan\left(\frac{S}{\hbar}\right) = \frac{\sum_{k=1}^{N} r_k \sin(s_k/\hbar)}{\sum_{k=1}^{N} r_k \cos(s_k/\hbar)}, \tag{11}$$

and the quantum potential will be given as

$$Q = -\frac{\hbar^2}{2m} \frac{\nabla^2 \left[\sum_{k,l=1}^{N} r_k r_l \cos[(s_k - s_l)/\hbar]\right]^{1/2}}{\left[\sum_{k,l=1}^{N} r_k r_l \cos[(s_k - s_l)/\hbar]\right]^{1/2}}, \tag{12}$$

which is quite different from

$$Q = -\frac{\hbar^2}{2m} \sum_{k=1}^{N} \frac{\nabla^2 r_k}{r_k}. \tag{13}$$

An example of this is provided by the harmonic oscillator, for which particles described by pure eigenstates are motionless, while those described by Gaussian wavepackets (linear combinations of eigenstates) move like classical particles in the same potential.

Finally, let us remark that non-separability is responsible for the non-locality observed in quantum correlated systems. Two very distant parts of a system described by the same quantum state, as happens for example with *entangled states*, maintain a strong correlation due to the presence of the quantum potential, which keeps the two parts connected. Notice that, as stated before, the action of the quantum potential can be very important far from the classical interaction region, where even its quantum intensity is vanishingly small in magnitude but not its spatial and temporal variation. This is another property characteristic of quantum systems, not observed in the classical theory of waves. Moreover, it is well known that the action of a classical wave depends on its magnitude and not on its form. In this new quantum

formalism, a different and opposite behaviour is found. By scaling the wavefunction with a constant a, we have that

$$Q' = -\frac{\hbar^2}{2m}\frac{\nabla^2(aR)}{aR} = -\frac{\hbar^2}{2m}\frac{\nabla^2 R}{R} = Q. \tag{14}$$

All of these facts imply that the notion of an asymptotic region, usually defined as the region where the external classical potential V is negligible, has to be revisited when quantum problems are considered in such a formalism.

2.3. The hydrodynamical interpretation of quantum mechanics

In close connection with the causal interpretation of quantum mechanics is the so-called hydrodynamical interpretation of quantum mechanics introduced by Madelung [34]. It also starts by introducing the wavefunction in polar form in the time-dependent Schrödinger equation, and taking into account the definition of the velocity field v of equation (6), and

$$\rho = R^2 = \Psi^*\Psi, \tag{15}$$

$$\boldsymbol{J} = \rho v = R^2 \frac{\nabla S}{m}, \tag{16}$$

where $\rho(\boldsymbol{r}, t)$ is the probability density and $\boldsymbol{J}(\boldsymbol{r}, t)$ is the quantum density current. By proceeding in this way, equations (3) and (4) transform to

$$\frac{\partial \rho}{\partial t} + \nabla \cdot \boldsymbol{J} = 0, \tag{17}$$

$$\frac{\partial v}{\partial t} + (v \cdot \nabla)v = -\frac{1}{m}\nabla(V + Q). \tag{18}$$

These equations constitute the formal basis of the hydrodynamical interpretation and are in direct correspondence with those of classical fluid mechanics if m is identified with the mass of a piece of fluid separated from the rest by a closed surface, $m\rho$ is the fluid density, and v is the velocity field of the flow [57]. However, unlike classical fluids, the 'fluids' of the hydrodynamical interpretation correspond to probability flows, with no material structure. They only characterize statistical events at each point in space and time, in spite of the fact that the time evolution of these events can be better understood when compared with the motion of ordinary fluids. Moreover, whereas the classical concept of fluid can be applied to describe the statistical behaviour of a macroscopic ensemble of particles, in quantum mechanics it is applied to single particles [58].

According to the preceding statements, equation (17) can be interpreted as the continuity equation for the quantum flow, which in terms of standard quantum mechanics translates into probability density conservation, while equation (18) represents the quantum Euler equation, analogous to the classical one for an ideal classical fluid (incompressible and non-viscous flow) when thermal effects are not taken into account. Indeed, if we consider the classical Euler equation for the component v_i of v,

$$\rho[\partial_t v_i + (v \cdot \nabla)v_i] = \rho f_i + \partial_j(-p\delta_{ij}), \tag{19}$$

where ∂_j is the spatial partial derivative with respect to the j-variable, f_i is the external force acting on the fluid along the i-direction, and p the fluid pressure, we see that the dynamics of the flow is determined by the influence of both an external force, and other internal one, given by $\rho^{-1}\partial_j(-p\delta_{ij})$, depending on the properties of the fluid. Now, equation (18) can be rewritten in the form of (19) as

$$\rho[\partial_t v_i + (v \cdot \nabla)v_i] = \rho f_i + \partial_j T_{ij}, \tag{20}$$

by defining a quantum stress tensor

$$T_{ij} = \frac{\hbar^2}{4m^2} \rho\, \partial_{ij} \ln \rho, \tag{21}$$

which is the quantal counterpart of the classical stress tensor $-p\delta_{ij}$, and whose explicit dependence on ρ can be easily obtained by using the following expression:

$$Q = -\frac{\hbar^2}{2m} \frac{\nabla^2 \rho^{1/2}}{\rho^{1/2}} = -\frac{\hbar^2}{2m} \left[\frac{1}{2}(\boldsymbol{\nabla} \ln \rho)^2 + \nabla^2 \ln \rho \right]. \tag{22}$$

An interesting hydrodynamical picture in phase space has been developed by Skodje *et al* [59]. By starting with the density operator for a pure state $\hat{\rho} = |\Psi\rangle\langle\Psi|$ satisfying the von Neumann relation, $i\hbar\, \partial_t \hat{\rho} = [H, \hat{\rho}]$, it can be shown that the diagonal coherent state representation of this expression, $\tilde{\rho}(\boldsymbol{q}, \boldsymbol{p}, t) = \langle\alpha|\hat{\rho}|\alpha\rangle$, becomes a phase space continuity equation:

$$\frac{\partial \tilde{\rho}(\boldsymbol{p}, \boldsymbol{q}, t)}{\partial t} = -\boldsymbol{\nabla}_p \cdot \tilde{\boldsymbol{J}}_p(\boldsymbol{p}, \boldsymbol{q}, t) - \boldsymbol{\nabla}_q \cdot \tilde{\boldsymbol{J}}_q(\boldsymbol{p}, \boldsymbol{q}, t), \tag{23}$$

where

$$\tilde{\boldsymbol{J}}_q(\boldsymbol{p}, \boldsymbol{q}, t) = \frac{1}{(\pi\sigma^2)^{N/2}} \frac{\hbar}{2m\mathrm{i}} \int \mathrm{d}\boldsymbol{x} \int \mathrm{d}\boldsymbol{y} \exp\{-[(\boldsymbol{x} - \boldsymbol{q})^2 + (\boldsymbol{y} - \boldsymbol{q})^2]/2\sigma^2\}$$
$$\times \exp[\mathrm{i}\boldsymbol{p} \cdot (\boldsymbol{y} - \boldsymbol{x})/\hbar][\boldsymbol{\nabla}_x \tilde{\rho}(\boldsymbol{x}, \boldsymbol{y}, t) - \boldsymbol{\nabla}_y \tilde{\rho}(\boldsymbol{x}, \boldsymbol{y}, t)], \tag{24}$$

$$\tilde{\boldsymbol{J}}_p(\boldsymbol{p}, \boldsymbol{q}, t) = \frac{1}{(\pi\sigma^2)^{N/2}} \int \mathrm{d}\boldsymbol{x} \int \mathrm{d}\boldsymbol{y} \exp\{-[(\boldsymbol{x} - \boldsymbol{q})^2 + (\boldsymbol{y} - \boldsymbol{q})^2]/2\sigma^2\}$$
$$\times \exp[\mathrm{i}\boldsymbol{p} \cdot (\boldsymbol{y} - \boldsymbol{x})/\hbar]\boldsymbol{K}(\boldsymbol{x}, \boldsymbol{y})\tilde{\rho}(\boldsymbol{x}, \boldsymbol{y}, t), \tag{25}$$

where σ is the coherent state width parameter, $\tilde{\rho}(\boldsymbol{x}, \boldsymbol{y}, t) = \langle\boldsymbol{x}|\hat{\rho}|\boldsymbol{y}\rangle$, and the kernel $\boldsymbol{K}(\boldsymbol{x}, \boldsymbol{y}) = -(1/2)\int_0^1 \mathrm{d}t\, [\boldsymbol{\nabla} V(\boldsymbol{w}+t\boldsymbol{z})+\boldsymbol{\nabla} V(\boldsymbol{w}-t\boldsymbol{z})]$, with $\boldsymbol{w} = (\boldsymbol{x}+\boldsymbol{y})/2$ and $\boldsymbol{z} = (\boldsymbol{x}-\boldsymbol{y})/2$. These two currents are not completely defined quantum mechanically, due to the ambiguity in the ordering when defining the flux operators, and a divergenceless single-valued vector function can be added and still fulfil the continuity equation. By an appropriate choice, one can profit from this fact when performing actual calculations. Equation (23) guarantees that $\tilde{\rho}(\boldsymbol{p}, \boldsymbol{q}, t)$ can be interpreted as an indestructible quasiprobability fluid in quantum phase space, which is driven by the current density $(\tilde{\boldsymbol{J}}_p(\boldsymbol{p}, \boldsymbol{q}, t), \tilde{\boldsymbol{J}}_q(\boldsymbol{p}, \boldsymbol{q}, t))$. Moreover, a phase space velocity field can be defined using $\tilde{\rho}(\boldsymbol{p}, \boldsymbol{q}, t)$, $\tilde{\boldsymbol{J}}_p(\boldsymbol{p}, \boldsymbol{q}, t)$, and $\tilde{\boldsymbol{J}}_q(\boldsymbol{p}, \boldsymbol{q}, t)$:

$$\tilde{\boldsymbol{J}}_p(\boldsymbol{p}, \boldsymbol{q}, t) = \tilde{v}_p(\boldsymbol{p}, \boldsymbol{q}, t)\tilde{\rho}(\boldsymbol{p}, \boldsymbol{q}, t), \tag{26}$$

$$\tilde{\boldsymbol{J}}_q(\boldsymbol{p}, \boldsymbol{q}, t) = \tilde{v}_q(\boldsymbol{p}, \boldsymbol{q}, t)\tilde{\rho}(\boldsymbol{p}, \boldsymbol{q}, t), \tag{27}$$

such that

$$\frac{\mathrm{d}\boldsymbol{p}}{\mathrm{d}t} = \tilde{v}_p(\boldsymbol{p}, \boldsymbol{q}, t), \tag{28}$$

$$\frac{\mathrm{d}\boldsymbol{q}}{\mathrm{d}t} = \tilde{v}_q(\boldsymbol{p}, \boldsymbol{q}, t), \tag{29}$$

and

$$\frac{\mathrm{D}\tilde{\rho}}{\mathrm{D}t} = \tilde{\rho}\boldsymbol{\nabla} \cdot \boldsymbol{v}, \tag{30}$$

where $\mathrm{D}/\mathrm{D}t$ indicates a derivative computed along a trajectory.

2.4. Quantum vortices

The hydrodynamical interpretation that we have just discussed can be easily connected with some relevant phenomena in quantum mechanics, such as superconductivity [60] and Bose–Einstein condensation [61], through the presence of vortices. The theory of quantum vortices, first described by Dirac in a classical paper [62] in which the existence of magnetic monopoles was suggested, has been described in detail in the literature (see, for example, [63, 64]), and some applications can be found in [65]. A more recent and explicit development of the quantum theory of magnetic monopoles, which constitutes a generalization of the concept of quantum vortex, can be found in [66]; also, related to this generalization there is the well-known Aharonov–Bohm effect [67].

The conditions leading to the formation of quantum vortices can be obtained from the fact that the complex character of the wavefunction implies the non-single valuedness of its phase:

$$S'(r, t_0) = S(r, t_0) + 2\pi n\hbar, \qquad n = 0, \pm 1, \pm 2, \ldots. \tag{31}$$

This multivaluedness can only take place at those points where $\Psi = 0$ (nodal points), where the smoothness of the wavefunction disappears, and then the value of S may undergo discrete jumps. According to equation (31), under these conditions the quantum density current (16) will vanish, but not the velocity field (6). If we now consider the circulation of v along a closed path, $\mathcal{C}$,

$$\oint_{\mathcal{C}} \mathrm{d}l \cdot v = \oint_{\mathcal{C}} \mathrm{d}l \cdot \frac{\nabla S}{m} = \frac{1}{m} \oint_{\mathcal{C}} \mathrm{d}S = \frac{2\pi n\hbar}{m}, \tag{32}$$

we find that this magnitude is quantized. Moreover, and by application of Stokes's theorem, we have

$$\int_{\Sigma} \mathrm{d}r \cdot (\nabla \times v) = \frac{2\pi n\hbar}{m}, \tag{33}$$

where Σ is the region enclosed by $\mathcal{C}$. This result indicates the localization of vortices when $n \neq 0$, which happens only at those points where the wavefunction presents nodes. At these points, the streamlines will be closed paths around the nodes, which is consistent with the fact that the quantum density current vanishes at those points and the impossibility of passing through the regions where $\rho = 0$. On the other hand, the velocity field v is irrotational in those regions free of quantum vortices.

2.5. The classical limit

Let us consider now the classical limit of quantum mechanics. We will understand this limit in a broad sense, that is, with actions (and other dynamical magnitudes) large compared to the value of $\hbar$. Notice that to recover classical mechanics it is not enough to define the limit $\hbar \to 0$, since this expression is not mathematically well defined unless it is clearly stated which other magnitudes are held constant in the process of approaching the limit [68, 69] (for this reason, this limit is usually referred as the semiclassical limit). This situation is well illustrated when considering the treatment of standing waves in BB theory. For example, in the case of a particle in a box where $\Psi(x) = L^{-1/2} \sin(px/\hbar)$, we have that the quantum potential, $Q = p^2/2m$, does not vanish when $\hbar \to 0$, and moreover

$$v = \frac{1}{m}\frac{\mathrm{d}S}{\mathrm{d}x} = 0, \tag{34}$$

contrary to the classical result, $v = p/m$.

The first connection that can be established between quantum and classical mechanics is the well-known Ehrenfest theorem. Since there are no trajectories in standard quantum

mechanics, one can expect a correspondence more in terms of averages over ensembles of classical trajectories. The result is derived by considering the time variation of the expectation value of a Hermitian operator A as

$$\frac{\mathrm{d}}{\mathrm{d}t}\langle A \rangle = \left\langle \frac{\partial A}{\partial t} \right\rangle + \frac{\mathrm{i}}{\hbar}\langle [H, A] \rangle. \tag{35}$$

By considering now r and p we have that

$$\begin{aligned}\frac{\mathrm{d}}{\mathrm{d}t}\langle r \rangle &= \frac{\langle p \rangle}{m}, \\ \frac{\mathrm{d}}{\mathrm{d}t}\langle p \rangle &= -\langle \nabla V(r) \rangle.\end{aligned} \tag{36}$$

Therefore the classical equations of motion are also valid for expectation values. However, this is not the classical limit, since equations (36) hold for any wavefunction. One way to obtain the classical limit is to consider the case in which the uncertainties, Δr and Δp, are small. If in equations (36) we could replace $\langle -\partial V(r)/\partial r \rangle$ by $-\partial V(\langle r \rangle)/\partial r$, then quantum averages would follow the classical equations. By expanding the 'force' $F(r) = \langle -\nabla V \rangle$ around the expectation value $\langle r \rangle$, it can be easily demonstrated that this is strictly true only for harmonic potentials, the error being of the order of

$$\left| \sigma^2 \frac{\partial^3 V/\partial r_i\, \partial r_j\, \partial r_k}{\partial V/\partial r_l} \right|, \tag{37}$$

for the case of a general potential function. The error term (37) is independent of $\hbar$ and vanishes for sufficiently narrow wavepackets or sufficiently smooth potentials. Only the first term in the Taylor expansion is felt and the Ehrenfest theorem is fulfilled. This result can be easily recovered from the hydrodynamical interpretation, equations (15)–(18), since it can be shown, by integrating by parts, that $-\langle \nabla Q \rangle = 0$. Note that the above results only concern average values and do not prove that quantum mechanics has the correct classical limit. In fact, for the quantum harmonic oscillator, the correction terms of equation (37) are exactly zero but it presents, however, a very different behaviour to its classical counterpart.

One step further, Ehrenfest's theorem, is reached by examining the oscillatory behaviour of the wavefunction, by considering only the effect of the phase:

$$\Psi(r, t) = \mathrm{e}^{\mathrm{i}\bar{S}(r,t)/\hbar}. \tag{38}$$

By expanding $\bar{S}(r, t)$ as a power series in $\hbar$,

$$\bar{S}(r, t) = \bar{S}_0(r, t) + \frac{\hbar}{\mathrm{i}}\bar{S}_1(r, t) + \left(\frac{\hbar}{\mathrm{i}}\right)^2 \bar{S}_2(r, t) + \cdots, \tag{39}$$

we obtain the equations for the different terms:

$$\begin{aligned}-\frac{\partial \bar{S}_0}{\partial t} &= \frac{1}{2m}(\nabla \bar{S}_0)^2 + V, \\ -\frac{\partial \bar{S}_1}{\partial t} &= \frac{1}{m}\left(\nabla \bar{S}_0 \cdot \nabla \bar{S}_1 + \frac{1}{2}\nabla^2 \bar{S}_0\right), \\ &\;\;\vdots\end{aligned} \tag{40}$$

The first equation (limit $\hbar \to 0$) is the classical Hamilton–Jacobi equation, so $\bar{S}_0$ corresponds to the classical action, and the others give the different corrections in $\hbar$; notice that all $\bar{S}_i$ are

real. Moreover, the probability density and associated probability current are given, to first order in $\hbar$, by

$$\rho(\boldsymbol{r}, t) \simeq e^{2\bar{S}_1(r,t)}, \tag{41}$$

$$\boldsymbol{J}(\boldsymbol{r}, t) \simeq \frac{\hbar}{m} \operatorname{Im}[\Psi^* \boldsymbol{\nabla} \Psi] = \frac{1}{m} e^{2\bar{S}_1} \boldsymbol{\nabla} \bar{S}_0, \tag{42}$$

both independent of $\hbar$. The associated semiclassical wavefunction (equation (39) with $\hbar = 0$) is best understood in one dimension, where it is given by the expression

$$\Psi(x, t) = \exp\left[\frac{i}{\hbar}\left(\pm \int^x dx' \sqrt{2m(E - V(x'))} - Et\right)\right], \tag{43}$$

which is a good approximation except in the vicinity of the classical turning points.

Let us consider now the limit $\hbar \to 0$ in phase space. For this purpose, we will use the quantum phase space hydrodynamical model [59] discussed above. As expected, the continuity equation reduces to the classical Liouville equation and the Lagrangian fluid trajectories approach the classical trajectories. The quantum deviations can be expressed as a power series in $\hbar$:

$$\tilde{\boldsymbol{J}}_q(\boldsymbol{p}, \boldsymbol{q}, t) = \frac{\boldsymbol{p}}{m}\tilde{\rho} + \frac{\hbar^2}{2m\sigma^2}\boldsymbol{\nabla}_p\tilde{\rho}, \tag{44}$$

$$\tilde{\boldsymbol{J}}_p(\boldsymbol{p}, \boldsymbol{q}, t) = -\tilde{\rho}\boldsymbol{\nabla}_q V(\boldsymbol{q}) - \frac{\sigma^2}{2}\frac{\partial \boldsymbol{\nabla}_q V(\boldsymbol{q})}{\partial q_i} - \cdots, \tag{45}$$

$$\frac{\partial\tilde{\rho}}{\partial t} = -\frac{\boldsymbol{p}}{m}\boldsymbol{\nabla}_q\tilde{\rho} + \boldsymbol{\nabla}_p\tilde{\rho}\boldsymbol{\nabla}_q V(\boldsymbol{q})$$
$$- \left(\frac{\hbar^2}{2m\sigma^2}\boldsymbol{\nabla}_q \cdot \boldsymbol{\nabla}_p\tilde{\rho} - \frac{\sigma^2}{2}\frac{\partial\boldsymbol{\nabla}_q V(\boldsymbol{q})}{\partial q_i} \cdot \frac{\partial\boldsymbol{\nabla}_p\tilde{\rho}}{\partial q_i} - \frac{\delta_{ij}\sigma^2}{4}\frac{\partial^2\boldsymbol{\nabla}_q V(\boldsymbol{q})}{\partial q_i \partial q_j} \cdot \boldsymbol{\nabla}_p\tilde{\rho}\right)$$
$$+ \cdots. \tag{46}$$

3. Computational methods

3.1. Quantum trajectories propagation

In order to calculate quantum trajectories and provide the causal interpretation for a given physical process, equations (3) and (4), or equivalently (17) and (18), must be solved together with equation (6). A wide variety of computational methods, based on different strategies, have been developed. They can be divided in two broad categories (we are not including here those cases in which an analytical solution for the Bohmian or the hydrodynamical equations can be derived, some examples of which can be found in [33]). The first group is constituted by those methods in which the hydrodynamical equations, (17) and (18), are solved directly. According to classical fluid dynamics, a very important point in this procedure is the choice of an appropriate reference frame where the partial derivatives are computed. Depending on the nature of this reference frame, two kinds of numerical scheme are possible: the *spatial* or *Eulerian scheme* [46] and the *material* or *Lagrangian scheme* [70, 71]. In the first one, the equations are solved in a fixed spatial grid or basis set and then the streamlines are obtained. Alternatively, if the Lagrangian description is considered, equations are set up in a reference frame moving with the fluid, that distorts as trajectories progress. This second method implies the evaluation of third-order spatial derivatives, which is a very difficult computational task, except for low-dimensional problems [47].

There is a second group of methods where the problem is tackled in two steps. In the first one, the wavefunction is obtained directly from the time-dependent Schrödinger equation

by a suitable time propagation scheme. Then, once $\Psi(\boldsymbol{r}, t)$ is known, quantum trajectories are calculated by means of (6). For simple systems the time evolution of the wavefunction can be easily obtained [72, 73] by using the so-called spectral methods, in which $\Psi(\boldsymbol{r}, 0)$ is projected onto the eigenstates of the corresponding Hamiltonian. For problems with more complicated potentials the evolution of $\Psi(\boldsymbol{r}, t)$ is obtained by more sophisticated methods, such as wavepacket propagation or the discretization methods. An interesting scheme is that of Heller [74], in which the wavefunction is given in terms of Gaussian functions, whose evolution in time is calculated by numerical integration. Grid methods, on the other hand, are based on a discretization of the system both in space and time. In relation to this, many efficient algorithms have been described in the literature [75–77] taking advantage of the excellent performance of the modern fast Fourier transform (FFT) methods [78]. Other authors [41] have used Feynman path integrals or Monte Carlo techniques [79] to compute Bohmian trajectories. Finally, a hybrid method, where some coordinates are considered classical while the others are described in terms of quantum trajectories, has recently been described by Gindensperger *et al* [51,52].

3.2. Wavepacket propagation—Heller's method

A simple method for propagating wavepackets in realistic systems is that proposed by Heller in 1975 [74]. The method is based on the fact that in a harmonic potential, Gaussian wavepackets maintain their Gaussian form, as the position and momentum of the centre evolve according to classical equations, in agreement with Ehrenfest's theorem (see equations (36) in subsection 2.5). Since the error of the method is of the order of σ^2 and the third derivative of the potential (see equation (37)), for sufficiently narrow wavepackets and a relatively smooth potential, one can assume a 'Gaussian ansatz' for all times and write the wavefunction in the form

$$\Psi(\boldsymbol{r}, t) = \exp\left\{\frac{\mathrm{i}}{\hbar}[(\boldsymbol{r} - \boldsymbol{r}_t)^\dagger \underline{\boldsymbol{A}}_t (\boldsymbol{r} - \boldsymbol{r}_t) + \boldsymbol{p}_t \cdot (\boldsymbol{r} - \boldsymbol{r}_t) + \gamma_t]\right\}, \tag{47}$$

where $\boldsymbol{r}_t$ and $\boldsymbol{p}_t$ are the position and momentum of the centre of the wavepacket at time t, $\underline{\boldsymbol{A}}_t$ is a complex square matrix where the imaginary part gives the spreading and the mode–mode correlations, and the (complex) variable γ_t contains the normalization constant and the $\boldsymbol{r}$-independent phase of Ψ. In order for Ψ_0 to be normalized, γ_0 must fulfil the relation

$$\gamma_0 = -\frac{\mathrm{i}\hbar}{4}\,\mathrm{Tr}\left(\ln\left[\frac{2\,\mathrm{Im}(\underline{\boldsymbol{A}}_0)}{\pi\hbar}\right]\right). \tag{48}$$

It can be easily verified that if $\langle\Psi|\Psi\rangle = 1$, then $\langle\boldsymbol{r}\rangle = \boldsymbol{r}_t$ and $\langle\boldsymbol{p}\rangle = \boldsymbol{p}_t$.

The equations of motion for the time-dependent parameters $\boldsymbol{r}_t, \boldsymbol{p}_t, \underline{\boldsymbol{A}}_t$, and γ_t are obtained by substituting equation (47) into the time-dependent Schrödinger equation:

$$\mathrm{i}\hbar\frac{\partial\Psi}{\mathrm{d}t} = H^{\mathrm{eff}}(t)\Psi, \tag{49}$$

where H^{eff} is the effective Hamiltonian

$$H^{\mathrm{eff}}(t) = \frac{\boldsymbol{p}^2}{2m} + V^{\mathrm{eff}}(\boldsymbol{r}, t), \tag{50}$$

where m is the mass, $\boldsymbol{p} = -\mathrm{i}\hbar\boldsymbol{\nabla}$, and V^{eff} is the approximate potential

$$V^{\mathrm{eff}}(\boldsymbol{r}, t) = V(\boldsymbol{r}_t) + V'(\boldsymbol{r}_t) \cdot (\boldsymbol{r} - \boldsymbol{r}_t) + \tfrac{1}{2}(\boldsymbol{r} - \boldsymbol{r}_t)^\dagger \underline{V}''(\boldsymbol{r}_t)(\boldsymbol{r} - \boldsymbol{r}_t). \tag{51}$$

After some algebra, one arrives at the following expressions:

$$\dot{r}_t = \left.\frac{\partial H}{\partial p}\right|_{p=p_t} = \frac{p_t}{m},$$

$$\dot{p}_t = -\left.\frac{\partial H}{\partial r}\right|_{r=r_t} = -V'(r_t),$$

$$\underline{\dot{A}}_t = -\frac{2}{m}\underline{A}_t{}^2 - \frac{1}{2}\underline{V}''(r_t), \tag{52}$$

$$\dot{\gamma}_t = \frac{i\hbar}{m}\,\mathrm{Tr}\,\underline{A}_t + p_t \cdot \dot{r}_t - E,$$

and the (conserved) energy is given by

$$E = \frac{p_t{}^2}{2m} + V(r_t). \tag{53}$$

At the same time as the wavefunction, $\Psi(r,t)$, is being propagated, the corresponding quantum trajectories can also be obtained by numerical integration of equation (6), given as

$$\dot{r} = \frac{\nabla S}{m} = \frac{1}{2mi|\Psi|^2}[\Psi^*\nabla\Psi - \Psi\nabla\Psi^*]. \tag{54}$$

Heller's method has been applied to atom–surface scattering problems [80] by representing the incoming plane wave,

$$\Psi_i(r, t=0) = \frac{1}{\sqrt{k_{z0}}}e^{ik_0 r} = \frac{1}{\sqrt{k_{z0}}}e^{-ik_{z0}z + iK_0 \cdot R}, \tag{55}$$

where $k_0 = (K, k_{z0})$ is the incident wavevector and R a vector parallel to the surface, such that $r = (R, z)$, in terms of Gaussian functions as

$$\Psi_i(r, 0) \simeq C\sum_{n=1}^{N}\exp\left[\frac{i}{\hbar}(r - r_0^n)^{\dagger}\underline{A}_0^n(r - r_0^n) + ik_0^n \cdot (r - r_0^n) + k_0^n \cdot r_0^n + \frac{i}{\hbar}\gamma_0^n\right]. \tag{56}$$

All Gaussian functions in this expansion share the same wavevector, k_0, but are centred on different points, r_0^n. The initial wavefunction is then propagated in time until it reaches the asymptotic region again, and then diffraction intensities can be calculated as the squared modulus of the S-matrix elements obtained by projection of the final wavefunction onto outgoing plane waves:

$$S_0^g = C'\sqrt{k_z^g}\sum_{n=1}^{N}\frac{\pi i}{(\det\underline{A}_0^n)^{1/2}}$$

$$\times \exp\left[-\frac{i\hbar}{4}(k_t^n - k^g)^{\dagger}(\underline{A}_0^n)^{-1}(k_t^n - k^g) - ik^g \cdot r_t^n + ik_0^p \cdot r_0^n + \frac{i}{\hbar}\gamma_t^n\right], \tag{57}$$

where g indicates the diffraction channel satisfying the diffraction condition for the corresponding final state, given by the kinematic equation

$$K_f = K_i + G, \tag{58}$$

where K_f and K_i are the parallel components of the final and initial wavevectors k_f and k_i, respectively, and G is the reciprocal-lattice vector.

3.3. Wavepacket propagation—grid methods

The use of grid methods to solve the time-dependent Schrödinger equation can be traced back to the work of Goldberg *et al* [81] on the penetration of one-dimensional square barriers and wells, where the results were displayed in the form of a 'movie'. The algorithm used for this purpose is based on a Crank–Nicholson scheme [78]. The method starts with the formal solution

$$\Psi(r, t) = e^{-iH(t-t_0)/\hbar}\Psi(r, t_0), \tag{59}$$

which is then approximated by the Cayley form

$$e^{-iH\delta/\hbar} \simeq \frac{[1 - iH\delta/2\hbar]}{[1 + iH\delta/2\hbar]} \tag{60}$$

with δ being a small enough time interval. This scheme is numerically stable and accurate to second order and, unlike other methods based only on $e^{\pm iH\delta/\hbar}$, has the desirable property of unitarity.

In order to improve the performance of methods like these, based on finite differences, other methods have been described in the literature. Probably, the most efficient nowadays are those based on the FFT [78], in which $\nabla^2\Psi$ is calculated by an N-dimensional FFT of Ψ followed by a multiplication by $-(K_1^2 + \cdots + K_N^2)$, and then an inverse N-dimensional FFT. This enhances the accuracy of the spatial representation, exhibiting an exponential convergence in sharp contrast with the power-law performance shown by finite-difference methods. For the propagation in time, different schemes have been proposed. Among them we should mention the second-order propagation method developed by Kosloff and Kosloff [76, 82], which will be used in our calculations in the next section. In such a scheme we have that

$$\Psi^{n+1} = \Psi^{n-1} - 2i\delta H\Psi^n, \tag{61}$$

where the superscript indicates the time step. Since this procedure needs the values of Ψ at two previously calculated points to initialize the solution, Ψ^1 is obtained from Ψ^0 with a second-order Runge–Kutta scheme.

A very interesting discussion about the convergence properties of some grid methods can be found in [83]. All of these methods use different approximations for the evolution operator $U(t) = e^{-iHt/\hbar}$, the global polynomial Chebyshev expansion [77] probably being one of the most widely used, because of its excellent performance.

4. Results

In this section we present some results concerning the diffraction of particles in different actual experimental situations, calculated within the BB theory, by propagating quantum trajectories. We start by considering the diffraction by a single slit and that by a double slit, which constitute paradigmatic experiments of quantum mechanics, for which accurate data, obtained in experiments with cold neutrons, can be found in the recent literature [4]. We then consider the case of the diffraction by N slits, a generalization of the previous problem, which has also been studied experimentally in diffraction experiments with very heavy particles, such as dimers, van der Waals clusters [5], and even fullerenes [6]. We should remark that, in spite of their apparent simplicity, there are some aspects of these experiments that, to the best of our knowledge, have not been satisfactorily explained yet. In particular, some fits are needed in order to obtain good agreement with the experimental measurements (full details of our calculations for slits and grating diffraction are deferred to a future publication). We proceed afterwards to consider the more complex phenomena of the scattering of He atoms with a
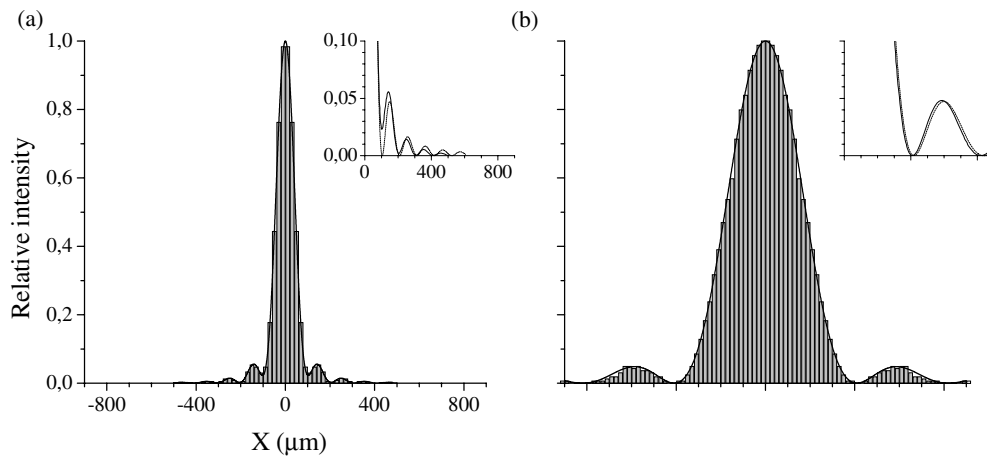
Figure 1. Intensity patterns for the diffraction of cold neutrons ($\lambda = 19.26$ Å) by a single slit of (a) 92.1 μm and (b) 23 μm, calculated with the S-matrix Heller method (——) and Bohmian trajectories (histogram). For comparison, we show in the insets the results ($\cdots\cdots$) obtained from Fraunhofer theory for one single slit, equation (62).

corrugated Cu surface where, contrary to previous cases, the classical interaction potential is non-zero. Finally, we present and discuss the scattering off surfaces with adsorbed molecules, by considering He colliding with CO–Pt(111). The study of such systems is very interesting since, in addition to its inherent importance in applied surface science, they can exhibit new types of relevant phenomenon such as trapping and surface resonances.

4.1. Single slit

In figure 1 we present some results for the intensity of diffraction of cold neutrons ($\lambda = 19.26$ Å) from a single slit corresponding to the experiments reported in figures 2 and 5 of [4], and where slits of widths $a = 92.1$ and 23 μm, respectively, were used. Our standard quantum calculation (full curve) has been performed by computing the diffraction intensity at a distance of $L = 5$ m away from the slit. The wavefunction is calculated by using the method due to Heller, which has been described in the previous section. Let us remark that in this case this computational method is exact since the classical potential is zero. The wavefunction consisted initially of 41 Gaussian wavepackets covering the full slit width so as to mimic a plane wave illuminating it. Aside from the different spreads in the observation plane, the main difference that can be observed between the two curves is that the minima of the first one, corresponding to the widest slit, do not go to zero, as predicted by the Fraunhofer formula [84]

$$I(\theta) \propto \frac{\sin^2[(\pi a/\lambda)\sin\theta]}{[(\pi a/\lambda)\sin\theta]^2}, \tag{62}$$

with $\theta = \tan^{-1}(x/L)$ being the observation angle (see the dotted curve in the insets of figure 1). This is due to the fact that only in case (b) is the observation made past the Rayleigh distance, $R = a^2/\lambda$, which is 4.4 m for case (a) and 0.27 m for case (b).

We have also calculated the corresponding diffraction patterns with the method of quantum trajectories. Our results (histograms) are superimposed in figure 1. The histograms were obtained by box-counting $\sim$3300 quantum trajectories with a narrow bin size of 20 μm, propagated by numerically integrating equation (6) with the wavefunction obtained as described
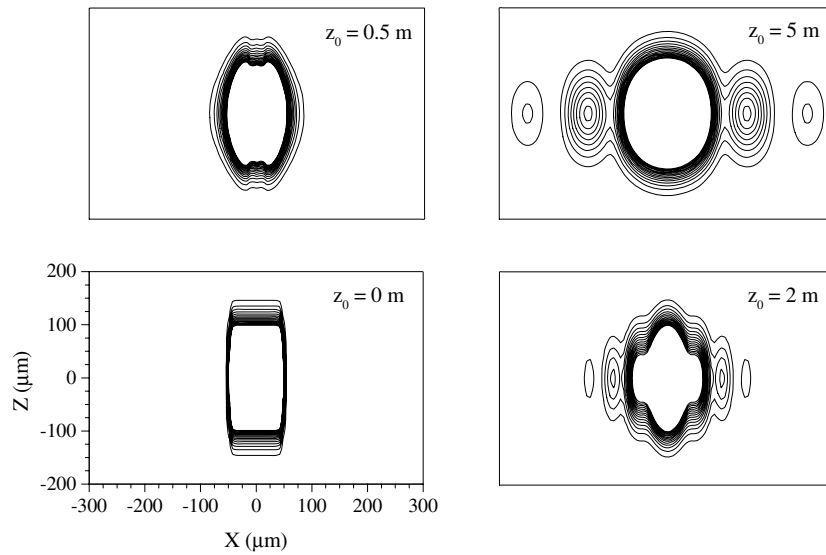
Figure 2. Snapshots of the time evolution of $|\Psi|^2$ corresponding to the case of figure 1(a). The position of the centre of the wavepacket, z_0, is given in each panel. In order to allow better appreciation of the diffraction effects, only contours below 10% of the density probability maximum are displayed.

before. As can be seen, the agreement between the quantum and the Bohmian trajectories results is excellent.

In figure 2 a series of snapshots showing the evolution of the wavepacket corresponding to figure 1(a) at different values of time is displayed; the position of the centre of the packet, z_0, at those instants is indicated in the figures. The initial width of the packet in the z-direction (perpendicular to the slit) has been chosen wide enough to ensure that the spread along this direction is negligible. In this respect, we remind the reader that the spread of a free wavepacket is given by

$$\sigma_z(t) = \sigma_0 \left[1 + \left(\frac{\hbar t}{2m\sigma_0^2} \right)^2 \right]^{1/2}. \tag{63}$$

In the figure, the formation of different diffraction maxima, as time progresses, is apparent.

In figure 3 the time evolution of the associated quantum potential, Q (see equation (5)), is shown. Lighter areas correspond to regions with higher values of the quantum potential. For $t = 0$, the potential value is everywhere equal to minus infinity, except for two (approximate) delta functions centred at the borders of the slit, with a zero plateau in between. On the other hand, the panels for other values of z_0 consist of a series of parallel fringes along the vertical direction, alternating maxima and minima of Q. This implies that when calculating the relative diffraction intensities, only trajectories along a line with constant z need to be sampled, since all trajectories having the same value of z_0, and differing in the value of x_0, are the same because they correspond to the same values of the quantum potential. Along the z-direction, Q is parabolic due to the Gaussian form of the wavepacket. Moreover, the change of intensity between fringes is fairly abrupt. This is very important because it is the derivative of this function that governs the dynamics of the associated quantum trajectories. It can be seen that, as time progresses and the wavepacket spreads, the distance between fringes increases. In an alternative plot, figure 4 displays two complementary views of Q in the form
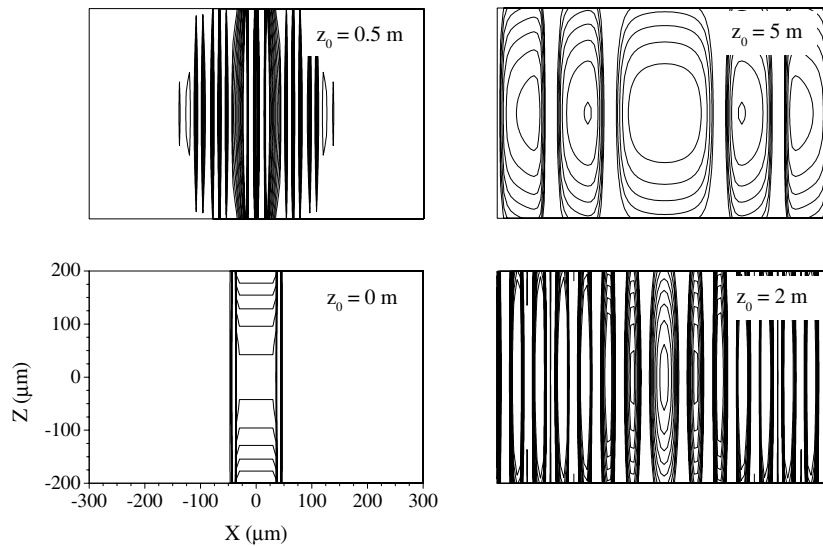
Figure 3. Snapshots of the quantum potential time evolution corresponding to the time steps of $|\Psi|^2$ given in figure 2.
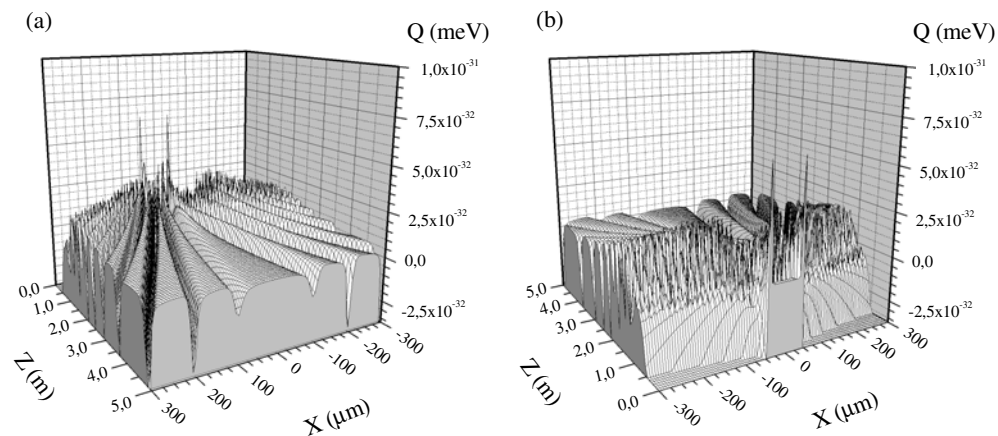
Figure 4. The quantum potential acting on the Bohmian trajectories of figure 5, viewed from the detection screen (a), and from the slit (b).

of slices computed as the quantum trajectories evolve (notice the difference from the previous representation). In these pictures, we see that the potential is essentially flat, but it has deep grooves aligned along the different final diffraction directions.

The corresponding quantum trajectories are plotted in figure 5. They follow lines that are essentially straight, except for at some points where they suddenly change direction. On examining them more closely, it can be appreciated that those points correspond to the regions in which the intensity of the quantum potential changes. This effect is easier to appreciate with the help of figure 4. Around the groove region, a strong 'quantum force' emerges. This force, acting each time that the quantum potential displays an abrupt variation, guides the different trajectories with successive kicks to the allowed Fraunhofer diffraction angles. In this problem the only existing force is of quantum origin, since the classical potential is zero everywhere.
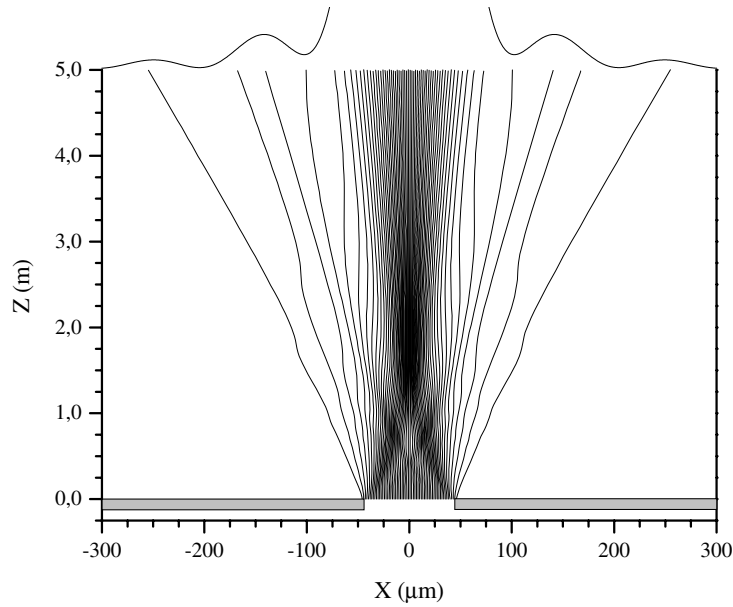
Figure 5. Bohmian trajectories corresponding to the case of figure 1(a). The intensity diffraction pattern has also been included at the top of the figure.

Another very interesting point concerning the quantum trajectories of figure 5 is associated with the wiggling pattern existing in the region near to the slit ($0 \leqslant z \leqslant 2$ m). This feature affects differently the various trajectories in the figure and it is the origin of a delay, making all trajectories arrive at the observation screen at the same time, despite the fact that those hitting it at the centre do it by taking shorter paths than those being detected at the borders.

To conclude this subsection, we present in figure 6 the quantum trajectories for case (b) of figure 1, corresponding to the narrowest slit used in the experiments of [4]. In this case the Rayleigh distance (0.27 m) is much smaller than the observation distance, and thus the region where the trajectories suffer important quantum forces is confined to an area much smaller than that of case (a). The quantum asymptotic pattern is then defined at a distance much closer to the slit.

4.2. Double slit

Similarly to what has been done in the previous section, we show in figure 7 the results of our computations for the two-slit diffraction experiment corresponding to figure 7 of [4], with $\lambda = 18.45$ Å, $a = 22.2$ μm, and the separation between slits $d = 104.1$ μm. In this case the relative intensity is a convolution of diffraction and interference, the first of these being given by the outer envelope of the curve (dotted curve) and the second by the enclosed oscillations (full curve). To highlight this effect we have also included in the figure the results obtained from a Fraunhofer calculation (dashed curve) with two slits [84]:

$$I(\theta) \propto \frac{\sin^2[(\pi a/\lambda) \sin \theta]}{[(\pi a/\lambda) \sin \theta]^2} \cos^2[(\pi d/\lambda) \sin \theta], \tag{64}$$

and with a single slit of the same characteristics (see equation (62)). It is important to note that the small discrepancy between the relative intensities calculated by the standard quantum
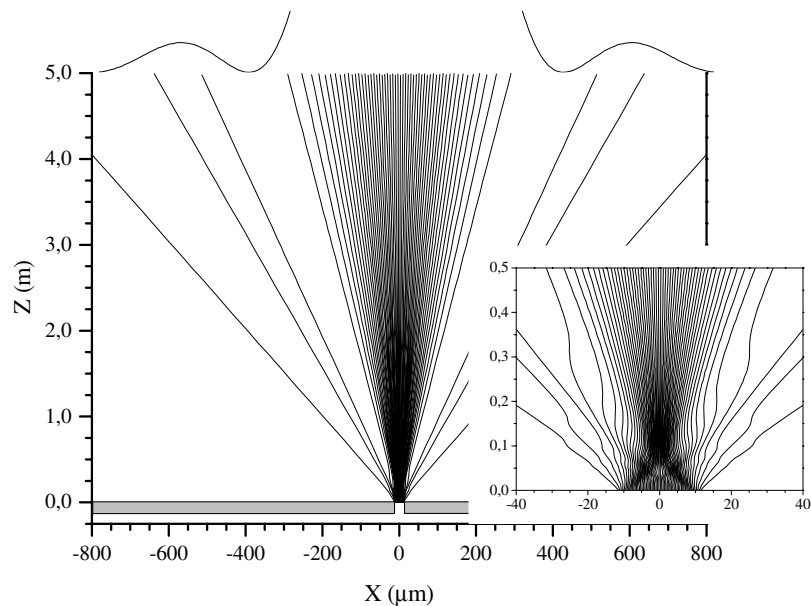
Figure 6. Bohmian trajectories corresponding to the case of figure 1(b). The inset is an amplification of the Fresnel region, close to the slit.

method and from quantum trajectories that is observed in figure 7 at $x = 0$ is misleading. It arises from the fact that the binning has been done in a symmetric fashion, not with any of the bins centred at that particular position. Similarly to what happened in the results of the previous subsection for one-slit diffraction, the minima of the curve do not go to zero, since again the conditions of the experiment are such that the Rayleigh distance (5.9 m in this case) is not attained.

In figure 8 the time evolution of $|\Psi|^2$ is shown. Initially, the wavefunction consists of 42 Gaussian wavepackets covering the two slits existing in the experimental set-up. This figure is highly illustrative, since it clearly shows that for times up to the point where the position of the packet reaches $z_0 \simeq 0.25$ m, only the separated effects of the diffraction due to each of the two slits are present, showing no interference between them. Notice that if this latter effect were not present, the Fraunhofer pattern would have already been almost completely formed at this point. The shape of the packet is essentially the sum of two contributions similar to that shown in figure 1 for the diffraction of a single slit. Afterwards, for longer times, the interference among the packets coming from different slits emerges, as can be appreciated in the remaining snapshots of figure 8. As time progresses, the interference pattern continues to build up until it reaches its final form in the asymptotic (Fraunhofer) region; see the snapshot at $z_0 = 5$ m where the different lobes associated with the different maxima in the diffraction pattern of figure 8 are clearly visible.

In figure 9 the corresponding quantum trajectories are plotted. Although they are similar to those found for the single-slit experiment, in this case the topology of the trajectories is much more complicated due to the existence of two effects: diffraction and interference, as mentioned above. Notice how these trajectories differ from those calculated by Philippidis *et al* [41] who used initially only one single Gaussian function per slit, thus precluding the existence of diffraction, an effect originated by the borders of the slits acting on the wavefunctions. The coexistence of diffraction and interference is also reflected in the shape of the quantum
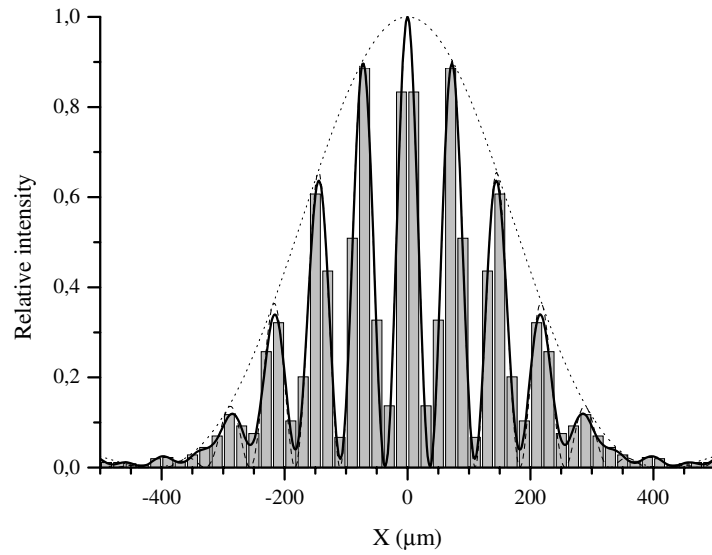
Figure 7. Intensity patterns for the diffraction of cold neutrons ($\lambda = 18.45$ Å) by two slits, 22.2 μm wide and separated by 104.1 μm, calculated with the *S*-matrix Heller's method (——) and Bohmian trajectories (histogram). For comparison, we include the results obtained from Fraunhofer theory for two slits, equation (64) (- - - -), and one slit with the same characteristics, equation (62) ($\cdots\cdots$).
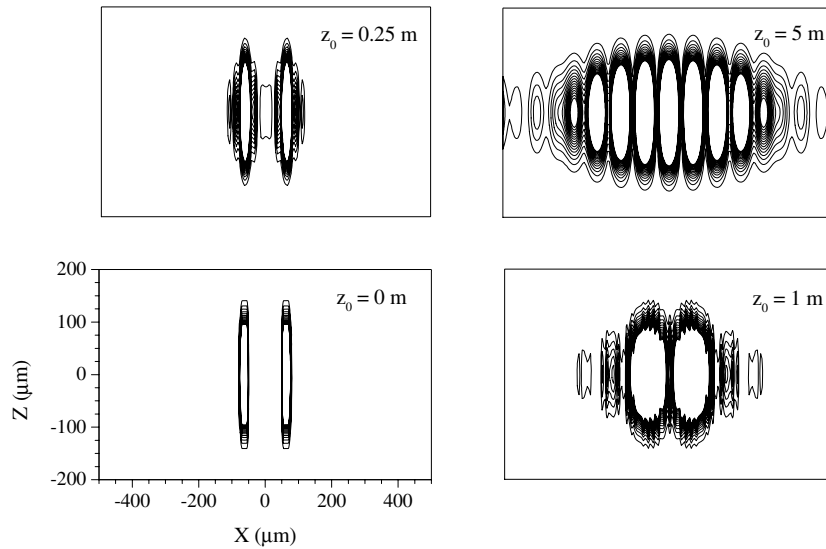

Figure 8. Snapshots of the time evolution of $|\Psi|^2$ corresponding to the case of figure 7. The position of the centre of the wavepacket, z_0, is given in each panel. In order to allow better appreciation of the diffraction effects, only contours below 10% of the density probability maximum are displayed.

potential, plotted in figure 10. Again, it consists of a series of plateaus where the trajectories are straight lines, crossed by a series of deep grooves, which are responsible for the changes in the direction of the trajectories, leading to the formation of the final intensity pattern.
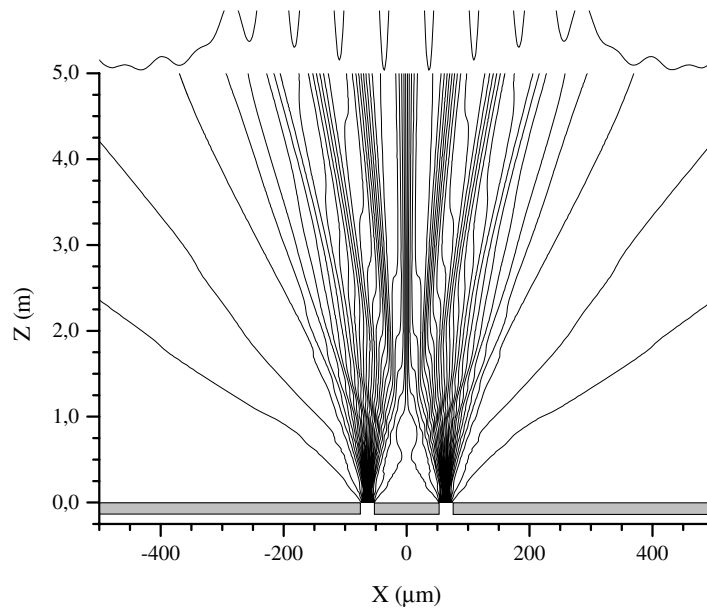
Figure 9. Bohmian trajectories corresponding to the case of figure 7. The intensity diffraction pattern has also been included at the top of the figure.
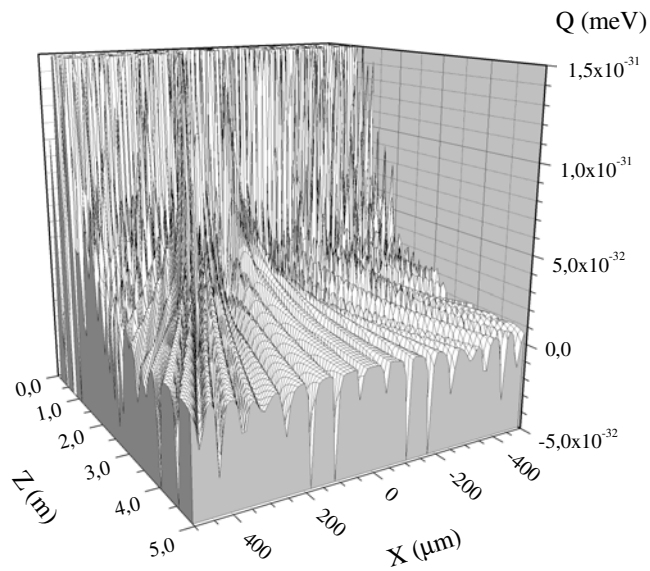
Figure 10. The quantum potential acting on the Bohmian trajectories of figure 9 viewed from the detection screen.

4.3. N slits

In this section we discuss the diffraction of particles by a series of slits (grating) as an intermediate step towards the consideration of particle scattering by corrugated metal surfaces, a topic that will be covered in the following subsections. In our case, we consider a sample with
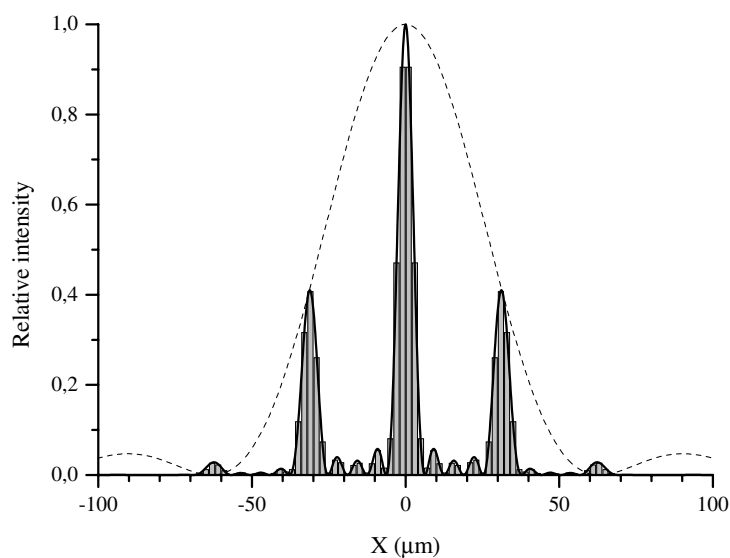
Figure 11. Intensity patterns for the diffraction of fullerenes ($v = 220$ m s^{-1}) by a series of five Gaussian slits, 50 nm wide and separated by 100 nm, calculated with the *S*-matrix Heller method (——) and Bohmian trajectories (histogram). For comparison, we include the results (- - - -) obtained from Fraunhofer theory for one single slit, equation (62).

five slits 50 nm wide and separated by a distance of 100 nm, in order to simulate the experimental conditions reported in [6], in which fullerene (C_{60}) molecules ($m = 1.19 \times 10^{-24}$ g) are passed through diffraction gratings at a speed of 220 m s^{-1}. The scattering of such heavy particles makes the classical–quantum correspondence regime accessible and, more interestingly, the existence of many internal degrees of freedom may facilitate the appearance of *decoherence* [53, 85] in a well-defined and controlled experimental situation.

Here all of our calculations have been performed placing a single Gaussian packet per slit, since the problem otherwise becomes very demanding computationally. This implies, as mentioned above, that only interference effects will appear in our results—it is impossible to analyse the associated diffraction phenomena. The corresponding intensity patterns calculated both with a standard quantum approach and quantum trajectories are recorded in figure 11, where it can be observed that the agreement between them is very good. The Fraunhofer limit corresponding to the diffraction of a single slit with the same characteristics (see equation (62)), and giving the envelope for our results, has also been included in the figure (dotted curve). The corresponding quantum trajectories are shown in figure 12, where the establishment of the Fresnel (close to the diffracting object, inset) and Fraunhofer (far from it) regions can be clearly appreciated. Moreover, it can be seen that the Fraunhofer pattern is established in this problem well before the wavepacket has had time to spread out completely.

4.4. Scattering of He atoms off weak corrugated Cu surfaces

Let us consider now the scattering of atoms by a weak corrugated metal surface. As stated before, this situation can be thought of as equivalent to the limit of diffraction through a grating of infinite dimension. As a working example, we will consider the scattering of He atoms off a Cu(110) surface; a case that has been extensively studied in the literature and for which a
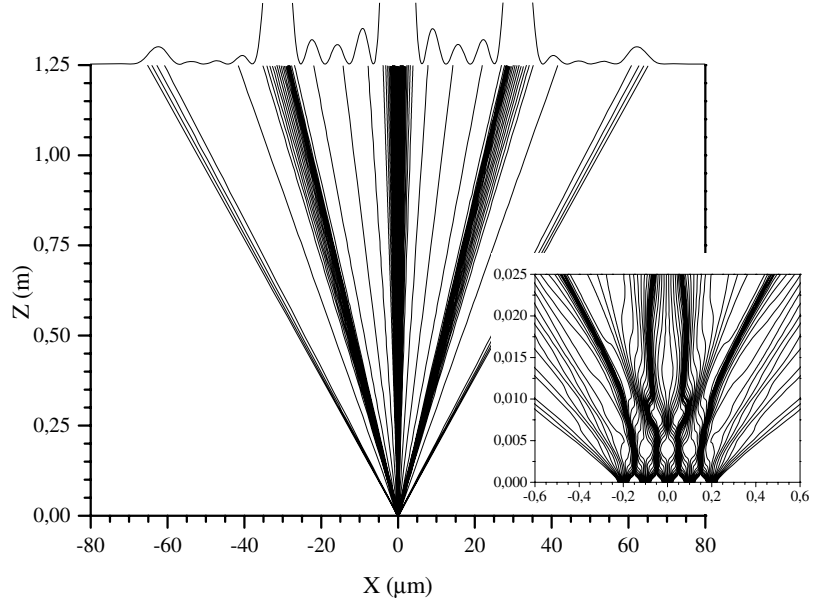
Figure 12. Bohmian trajectories corresponding to the case of figure 11. The inset is an amplified view of the Fresnel region, close to the slits.

two-dimensional realistic interaction potential exists [26]. This potential is described by the corrugated Morse function

$$V(x, z) = V_M(z) + V_C(x, z), \tag{65}$$

V_M being the Morse function

$$V_M(z) = D_s[e^{-2\alpha(z-z_m)} - 2e^{-\alpha(z-z_m)}], \tag{66}$$

and V_C the coupling term

$$V_C(x, z) = D_s e^{-2\alpha(z-z_m)}[0.03\cos(2\pi x/a) + 0.0004\cos(4\pi x/a)]. \tag{67}$$

The coordinates z and x are defined as perpendicular and parallel to the surface, respectively, and the parameters involved have the following values: $D_s = 6.35$ meV, $\alpha = 1.05$ Å^{-1}, $z_m = 0$, and $a = 3.6$ Å. The associated time-dependent wavefunction, $\Psi(x, z, t)$, has been calculated by means of the Heller method, starting with the centre of the packet at a distance sufficiently far from the surface ($z_0 = 12$ Å), with x_0 distributed according to the statistical weight $|\Psi(x, z_0, t = 0)|^2$. All calculations have been performed at an energy of $E = 21$ meV and angles of incidence of $\Theta_i = 0°$ [49] and $15°$ (angles are measured from the normal to the surface plane).

Two important technical points must be taken into account when applying Heller's method to atom–surface scattering. First, the wavepacket has to be spread over a spatial region large enough to allow an adequate sampling of the surface details (corrugation). As has been done in previous subsections, this can be accomplished by combining a number of Gaussian functions to form a suitable initial wavefunction. Secondly, the value of the imaginary part of the shape matrix, $\underline{A}_0$, must be chosen such that a minimum spread of the packet when hitting the surface (where the strongest interaction is felt) takes place. In this sense, it is important to remark that the calculation carried out at $\Theta_i = 15°$ is more complicated and constitutes a sterner computational test of the application of Heller's method than the previously

Table 1. Positions of the different diffraction order (n) intensity peaks for He–Cu(110) scattering at $E = 21$ meV, calculated with the S-matrix Heller method (Q), and the kinematic equation (68) (KE).

	$\Theta_i = 0°$		$\Theta_i = 15°$	
n	Θ_n^Q	Θ_n^{KE}	Θ_n^Q	Θ_n^{KE}
−4	—	—	−60.99°	−57.36°
−3	−55.48°	−55.66°	−36.21°	−34.53°
−2	−32.99°	−33.40°	−17.30°	−16.96°
−1	−15.98°	−15.98°	−1.31°	−0.94°
0	0.00°	0.00°	14.70°	15.00°
1	15.98°	15.98°	31.88°	32.28°
2	32.99°	33.40°	51.69°	54.02°
3	55.48°	55.66°	—	—

reported calculation [49, 50] where the scattering was studied only at normal incidence. For one thing, the intensity pattern at $\Theta_i \neq 0$ is asymmetrical, more complex, and, more importantly, 'different parts' of the incident front associated with the initial wavefunction collide with the metal surface at different instants of time (see the discussion below) and thus the control of the spreading, necessary in Heller's method, is more difficult.

In table 1 we present the results for the diffraction intensity pattern of the He–Cu(110) scattering calculated with the standard S-matrix quantum method together with the positions of the peaks calculated with the kinematic equation (see equation (58)):

$$\Delta K = K_x^f - K_x^i = k_i \sin \Theta_f - k_i \sin \Theta_i = \frac{2\pi n}{a}, \tag{68}$$

where n is an integer giving the diffraction order. As can be seen, the agreement for normal incidence is very good, while a small deviation is observed in the results for $\Theta_i = 15°$, which are nevertheless still good. As discussed above, this is due to the fact that the performance of Heller's method is poorer in the second case. In the rest of this subsection, we will concentrate on the results obtained for oblique incidence.

In figure 13 the convergence process for the results obtained by considering different numbers of Gaussian functions to approximate the incident plane wave is displayed. In all cases shown in the figure, the same number of Gaussian packets covering each unit cell (ten functions per cell) is used; thus varying the number of cells to improve convergence. As can be seen in the figure, as this number is increased the peaks become narrower, and their positions better defined. Moreover, it can be inferred that an initial wavefunction covering a minimum of ten cells is required in order to obtain good results in our calculations.
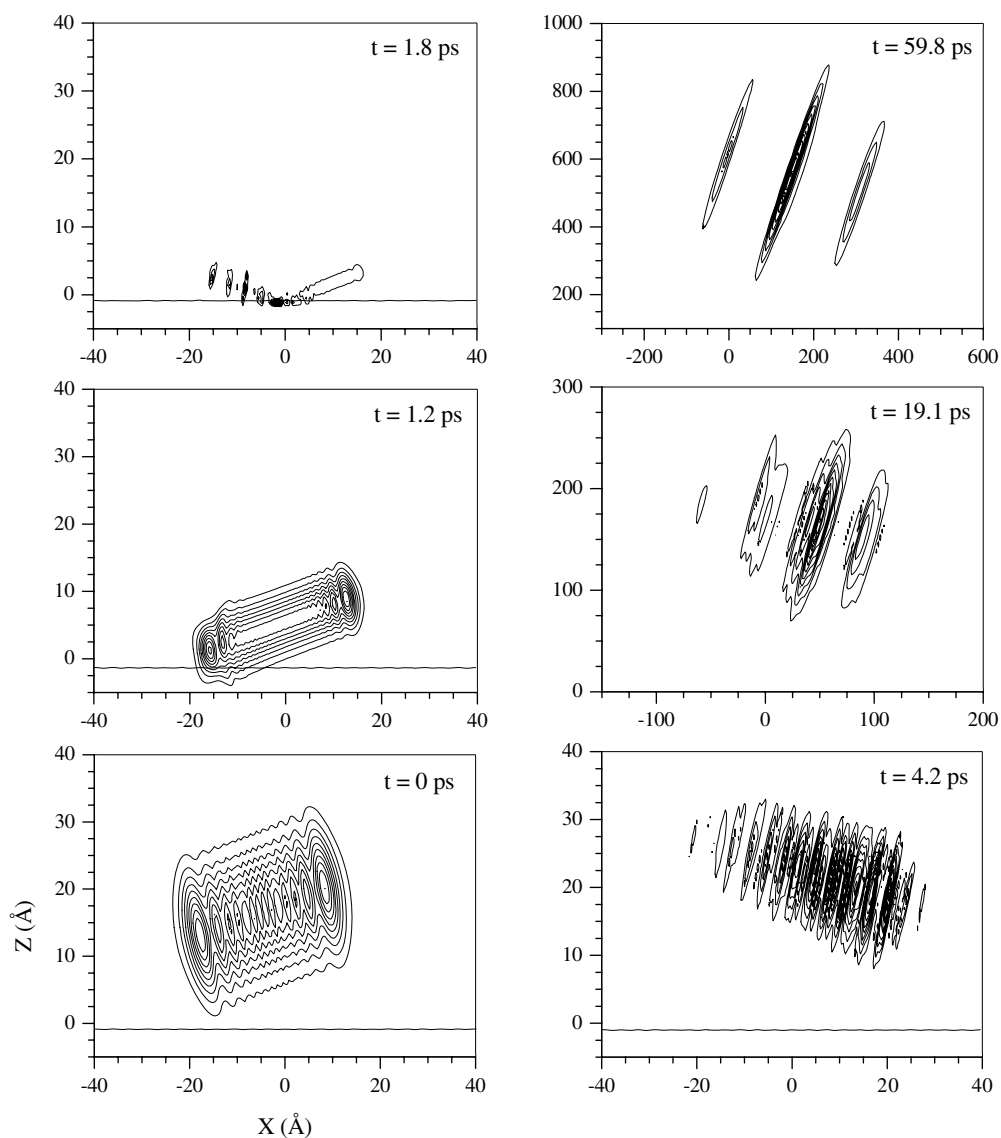
In figure 14 snapshots of the evolution of the wavepacket, computed by Heller's method, at different instants of time are shown. In the first part of the collision, the packet becomes more concentrated as it approaches the Cu surface, so when it hits the surface ($t \simeq 1.8$ ps) the spread is minimum. This effect is due to the initial value chosen for the imaginary part of the shape matrix, as explained before. At this point the wavefunction shows an incident part, fairly intact, at the right of the point $x = 0$, and a scattered one, more complex, at the left of that point. Afterwards, the packet becomes completely dispersed by the strong interaction, breaking up into different pieces which evolve over time, producing in the asymptotic region ($t \simeq 59.8$ ps) three main contributions corresponding to the specular and two first-order diffraction channels, the intensity of the former being much greater than those of the others.

The corresponding quantum trajectories are displayed in figure 15 for three different ranges of the z-coordinate. To make the picture clearer, we have not plotted the incident part of the trajectories, where due to the lack of interaction nothing interesting happens. In the first panel

(d)

(c)

(b)

(a)

Relative intensity

1,0

0,8

0,6

0,4

0,2

0,0

-60 -40 -20 0 20 40 60

Θ_{def} (deg)
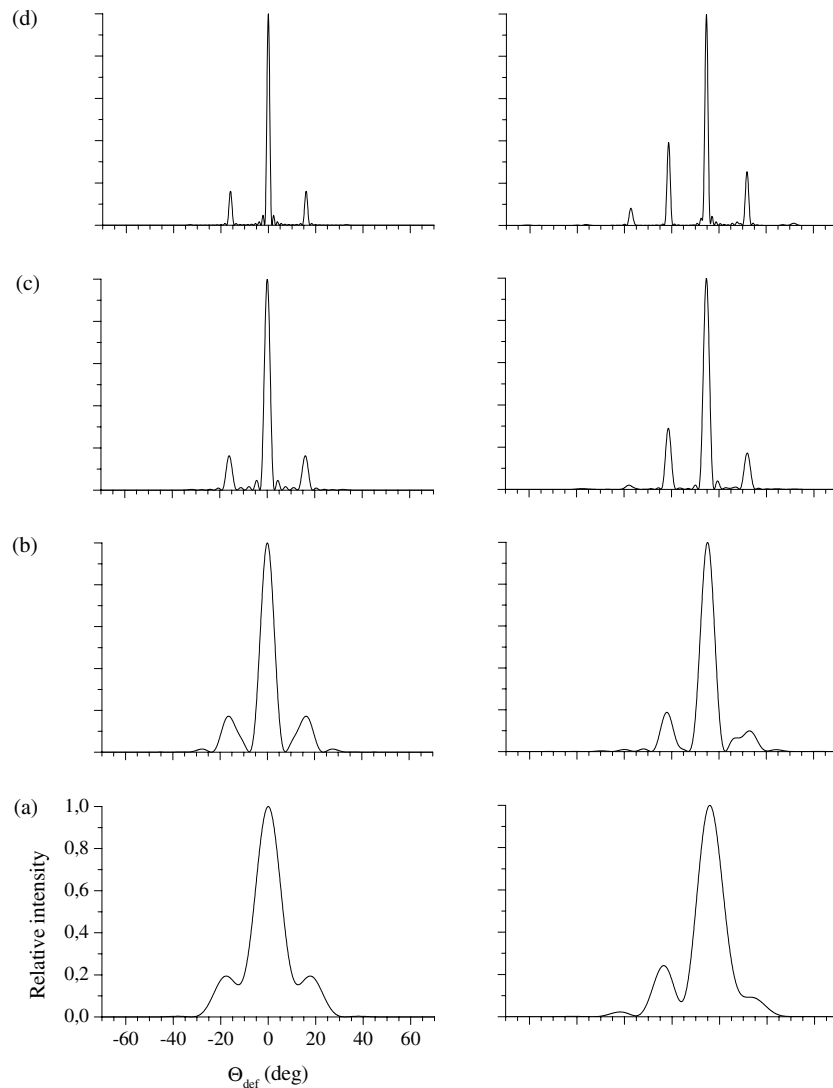
Figure 13. Convergence of the intensity patterns for the He–Cu(110) scattering at $E = 21$ meV with the number of Gaussian functions, N, used to describe the initial plane wave in the calculation: (a) $N = 10$, (b) $N = 20$, (c) $N = 50$, and (d) $N = 100$. In all cases a 'density' of ten Gaussians per unit cell is maintained. The results on the left and right tiers correspond to incident angles of $\Theta_i = 0°$ and $15°$, respectively.

(part (a) of the figure) we show the region closest to the Cu surface, where the effect of the corrugation occurs. To gauge this effect we include the equipotential line corresponding to $E = 21$ meV. The trajectories show undulations that can be correlated with the shape of the corrugation function, accumulating on top of the minima of this function and becoming more sparse over the corresponding maxima. These trajectories avoid crossing (at the same moment of time), and although the overall pattern is more irregular than in the case of normal incidence reported in [49], this is mainly due to the loss of symmetry, and many similarities between the two cases are found. In panel (b) of the figure, we are further from the surface. The undulatory

Figure 14. Snapshots of the time evolution of $|\Psi|^2$ corresponding to the case of figure 13 for $N = 100$ and $\Theta_i = 15°$.

pattern has disappeared and the trajectories are more rectilinear, although some changes of direction are still visible. The incipient possible diffraction channels are noticeable from the difference in the density of trajectories. Finally, panel (c) corresponds to the asymptotic region where the z-coordinate (and consequently the x-coordinate) has attained a very big value. In the (c) panel the trajectories are completely rectilinear and the diffraction channels are totally defined. At this point several comments are in order. In the first place, regions (a) and (c) are completely analogous to the Fresnel and Fraunhofer regions that appear in the classical optics of diffraction phenomena. The parallel is perfect, since in the former, or near-field region, information about the form of the diffracting object is obtained, while in the latter, or far-
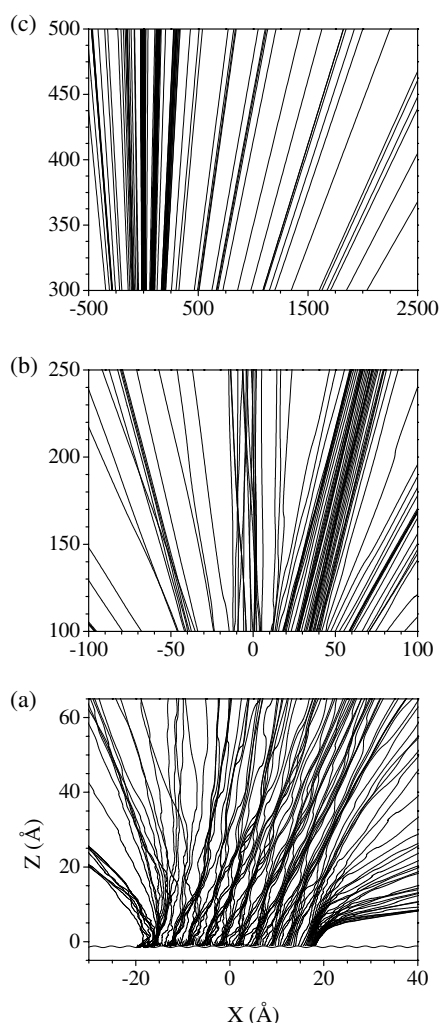
Figure 15. Bohmian trajectories corresponding to the case of figure 13 for $N = 100$ and $\Theta_i = 15°$. The different panels show the three regions of interest in the scattering process: (a) Fresnel or near-field region, (b) transition or intermediate-field region, and (c) Fraunhofer or far-field region.

field region, the effects (redistribution of momenta) produced by that object are visible. The transition between these two regions, taking place for classical optics at around the Rayleigh distance, is not well defined as the intermediate region in panel (b) shows. Another point worth making about figure 15 is that the 'quantum asymptotic distance', defined as the region in which the quantum trajectories are free from any force, is much bigger—actually by two orders of magnitude in the case of the He–Cu scattering—than the classical one, defined, as usual, as the distance at which the classical potential is (practically) flat (~12 Å in our case). Finally, it is interesting to note that quantum trajectories allow a very rigorous definition of corrugation, as the loci of the corresponding turning points. Usually classical trajectories are used for this purpose, and thus the corrugation is determined by the electronic density at the surface and is calculated as an equipotential line. The use of quantum trajectories instead provides a more reliable method of calculating this function, since it automatically contains all quantum effects discarded in the customary procedure.
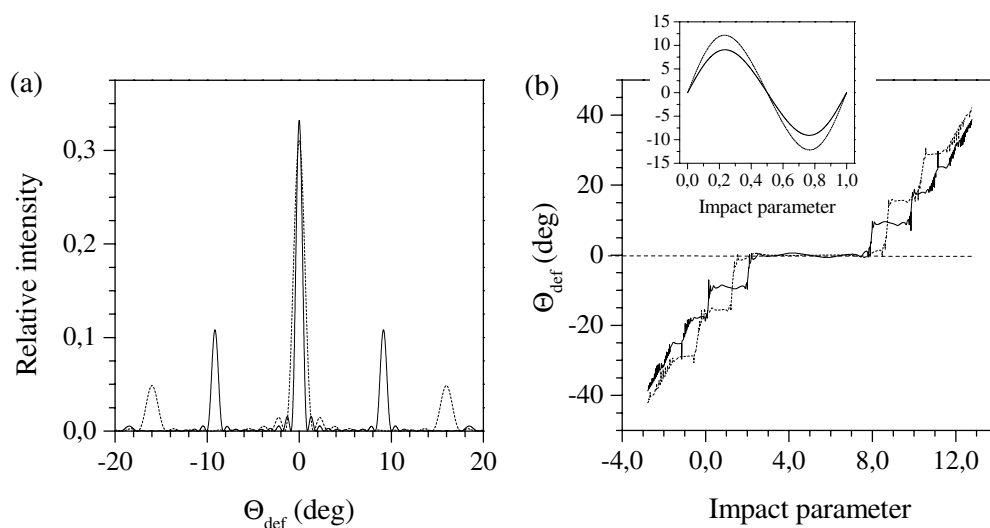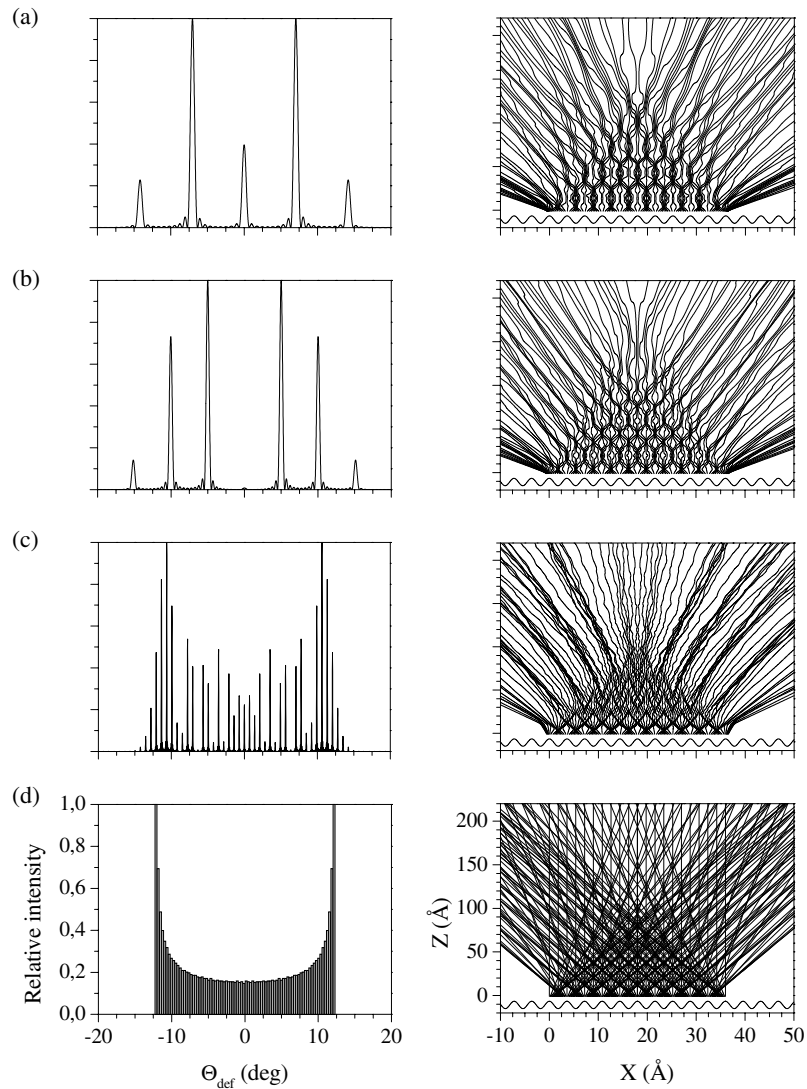
Figure 16. The intensity diffraction pattern (a) and QD function (b) for the He–Cu(110) scattering at $E = 21$ meV (———), and $E = 63$ meV ($\cdots\cdots$) at normal incidence. The impact parameter is given in units of the unit cell, 3.6 Å. The corresponding classical deflection functions are also plotted in the inset of panel (b).

4.5. Classical limit of atom–surface diffraction

In the interpretation of scattering experiments, like those described in the previous section, it is common to resort to classical or semiclassical mechanics to assign some particular features (diffraction and rainbow peaks) appearing in the corresponding measurements. This is even more relevant in the experiments with very heavy particles described in the introduction to this section. However, this procedure must be applied with caution since the semiclassical limit is highly non-uniform.

In this subsection we will explore such a limit in the He–Cu(110) scattering that we have just described, using the causal methodology implied in the BB theory. To do this, we select some conditions such that a rainbow effect exists, since for this effect there is a clear and unique correspondence between quantum and classical features, the latter being the limiting case of the former. Classically, rainbows are marked by the presence of caustics, at which the primitive semiclassical wavefunction breaks down. This singularity is replaced, quantum mechanically, by an intensity maximum in the angular distribution, and the quantum rainbow condition occurs when the classical rainbow coincides with a Bragg channel. In this respect, it has been argued that rainbow features should be associated with the whole diffraction pattern instead of a very high-intensity diffraction peak, which does not necessarily correspond to the diffraction channel displaying the rainbow [86].

The correspondence between quantum and classical mechanics can be mathematically expressed within the BB theory as the limit $Q \to 0$. In our case we will achieve this limit by considering increasing values of the mass of the impinging atom; in particular, we will consider the rare-gas-atom sequence He, Ne, Ar, He*, the latter being a fictitious atom with a mass $m_{He^*} = 500\, m_{He}$. In this process, we will keep the same interaction potential, in spite of the fact that the attractive well and the corrugation are expected to become larger as m increases. We will minimize this effect in our final conclusions by considering scattering at normal incidence, and with incident energies of the order of the potential well.

Figure 17. The intensity diffraction pattern (left tier) and quantum trajectories (right tier) for He–Cu(110) scattering at $E = 21$ meV and normal incidence for particles with masses equal to: (a) m_{Ne}, (b) m_{Ar}, (c) $m_{He^*} = 500\, m_{He}$; and (d) classical results. To make the comparison easier, all intensities have been normalized to their maximum values.

In figure 16 we show the results for the scattering of He atoms off Cu(110) surfaces at $E = 21$ and 63 meV. Panel (a) gives the diffraction pattern calculated using the S-matrix method described in the previous section, and in panel (b) the quantum deflection (QD) function, calculated from the final deflection angle of the quantum trajectories, is displayed; the inset shows the classical (CD) counterpart (for one unit cell). The impact parameter is given in units of the unit cell, 3.6 Å. Since the diffraction pattern has three main peaks, corresponding to the zero (specular) and first diffraction orders, at $0°$ and $\pm 15.9°$ for $E = 21$ meV, and $0°$ and $\pm 9.2°$ for $E = 63$ meV, respectively, and the CD function shows extrema (rainbow angles) at $\pm 12.2°$ and $\pm 9.2°$ for the same energies, we can conclude that the first-order peaks at $E = 63$ meV

(a)

(b)

Impact parameter

(c)
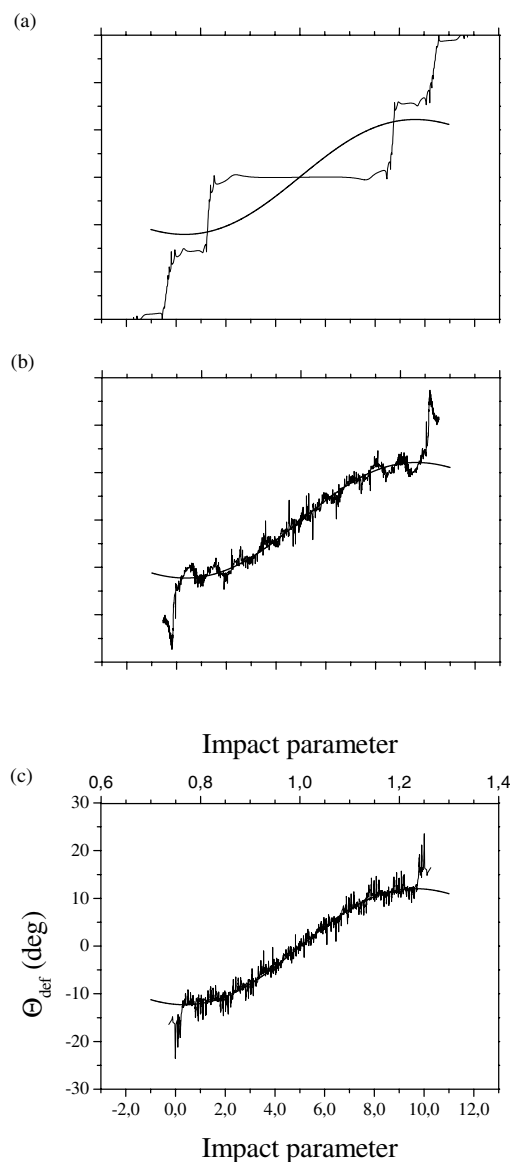
Figure 18. Quantum (thin solid curve) and classical (thick solid curve) deflection functions for He–Cu(110) scattering at $E = 21$ meV and normal incidence for particles with masses equal to: (a) m_{He}, (b) $m_{He*} = 500 \, m_{He}$, and (c) $m_{He**} = 1000 \, m_{He}$. The impact parameter is given in units of the unit cell, 3.6 Å. The classical results have been normalized to the width of the initial wavepackets.

display a quantum rainbow feature, and the whole diffraction pattern is associated with the surface rainbow. This is also responsible for the increment in the integrated intensity of the specular diffraction peak and the decrease in the first-order peaks with respect to the results for 21 meV that are observed.

In the semiclassical picture, the trajectories contributing to the 15.9° peaks are classically forbidden, although energetically allowed (see Guantes *et al* in [32]). In the BB formalism, however, it is not necessary to resort to such trajectories, since all quantum effects are taken into

account. The QD function of figure 16 presents a ladder-type shape connected with the Bragg angles, in clear contrast with the CD function. Each step comes from trajectories launched at different positions on the initial wavepacket, the central one being associated with the specular one. Moreover, the density of trajectories in each of the steps weighted with the probability arising from $\Psi(x, z_0, 0)$ is proportional to the corresponding diffraction intensity.

Let us consider now calculations performed at different values of the impinging atom mass for an energy of 21 meV, the quantum rainbow condition not being fulfilled. The results are shown in figure 17, where S-matrix intensities are shown in the left panels, and the associated quantum trajectories in the right ones. These trajectories are only plotted in the region close to the surface (Fresnel zone), and again to avoid making the figure too complicated, only the outgoing parts have been plotted. The classical results are also shown at the bottom for comparison. The S-matrix results show an increasing number of peaks as m increases, approaching the classical limit as this happens. At the same time, the specular peak gradually disappears (consider the upper part of figure 16(a) as the first member in this series of results), and an oscillatory behaviour in the intensity of the peaks is observed. Turning to the right column, we see that as this happens, the topology of the quantum trajectories becomes more and more complex, the paths being more convoluted. This can be explained within the hydrodynamical interpretation of quantum mechanics (see section 2.3): light particles move within laminar flux, whereas as m increases the turbulent regime starts. Furthermore, this convoluted pattern evolves clearly towards the classical results, although an important difference remains. In the classical case, the CD function is periodic, with the trajectories covering densely the interval between two rainbow angles where caustics exist. The Bohmian trajectories for high values of m, on the other hand, are bunched in groups pointing in the direction of the allowed Bragg angles and, especially, the rainbow angles. The mechanisms of appearance of the rainbows in the two theories are then quite different. Classically, two rainbows are originated at each unit cell, and the results then repeat periodically; while quantally, the accumulations are caused by the trajectories at the borders of the illuminated area. This is a consequence of the non-local character of Q, which does not disappear at the high values of m considered in our calculations. This is analogous to what happens with the strong oscillations of the standard quantum mechanics S-matrix calculations, in contrast with the smooth shape of the classical form. Finally, we should remark that in the limit $m \to \infty$ that we are considering, the pattern formed by the quantum trajectories becomes remarkably close to the classical one.

The previous results pose the fundamental question of how, and following what mechanism, the classical limit emerges from the quantum results, according to the correspondence principle. This can be further analysed by considering the results of figure 18, where we show the QD function calculated with a lot of detail ($\sim$3000 trajectories have been used) for three values of m, corresponding to m_{He}, $m_{\text{He}^*} = 500\, m_{\text{He}}$, and $m_{\text{He}^{**}} = 1000\, m_{\text{He}}$, respectively. Here again the impact parameter is given in units of the unit cell, 3.6 Å. We see a clear transition from a discrete, ladder-type shape, typical of the quantum regime, to a more continuous dependence, characteristic of the classical behaviour. More importantly, the average of the QD function is in excellent quantitative agreement with the CD function for He, when normalized in width to the number of unit cells spanned by the initial wavefunction. The existence of (slow) modulations in the QD function is an indication of how the surface corrugation is 'seen' by the initial wavepacket, while the fastest ones are a direct consequence of the effect of the quantum potential.

The conclusion of this subsection is clear. Our results unambiguously confirm the clear influence of the classical behaviour in the quantum He–Cu scattering results: the whole diffraction pattern is determined by the rainbow condition, even in the case considered. At the same time, the non-local character of the quantum dynamics is always preserved.
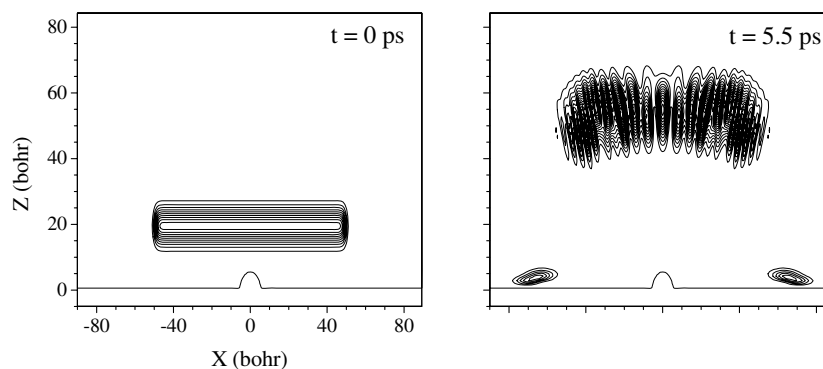
Figure 19. The incoming plane wave (left) and outgoing scattering wave (right). Notice that part of the intensity is trapped by the Morse potential on the Pt surface, leading eventually to the formation of SAR mediated by defects.
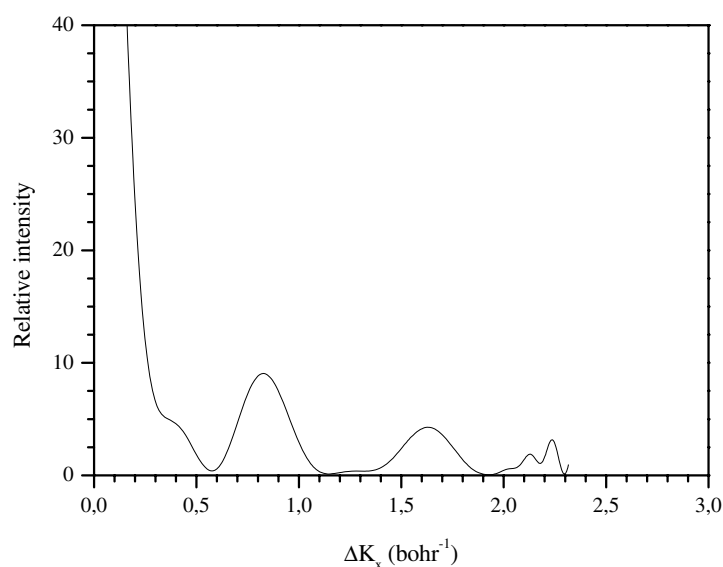
Figure 20. The final scattering distribution, obtained from wavepacket propagations, for a 2D, soft interaction potential between He atoms and CO adsorbed on a Pt(111) surface at $\Theta_i = 0$ and $E_i = 10$ meV.

Very recently, an experiment with an interferometer at the quantum–classical boundary has been reported [87] to illustrate the quantum mechanical principle of complementarity.

4.6. Adsorbates He–CO/Pt(111)

In contrast to well-ordered surfaces, surfaces with defects disrupting their otherwise perfect periodicity can be found. When He atoms probe a solid surface, the corresponding angular distribution displays peaks in between the Bragg peaks. This type of scattering is called diffuse elastic scattering. Sometimes it is also called incoherent, since no phase relationship exists between particles scattering off different defects. Large-angle diffraction oscillations in

the intensity of He atoms elastically scattered from randomly stepped Pt(111) surfaces and estimates of single adsorbate sizes (CO on Pt(111)) were reported a long time ago [88]. Since these earlier studies, the CO–Pt(111) system has come to be seen as a prototype system for experimentalists and theoreticians. Observations are made more readily at low surface temperatures and coverages—to prevent ordered island formation reducing the inelastic background contribution. Furthermore, working at high incident energies of He atoms, while good for theory, is not so convenient for experiments, because again the inelastic contribution is increased and the resolution is poorer. The CO molecule is known to adsorb preferentially at step sites.

Angular intensity distributions are usually measured as a function of the parallel momentum transfer, ΔK, for a given direction and defined similarly to in equation (68). Large diffraction angles (or, equivalently, large ΔK values) are mainly determined by the repulsive part of the interaction potential. Analogously, scattering intensities at small values of ΔK are dominated by the attractive, long-range part of the potential. Finally, interference oscillations and rainbow peaks are the basic features observed in this type of angular distribution. Some controversy can be found in the literature regarding the assignment of the different types of such oscillations. From a theoretical point of view, the different methods applied to the scattering of atoms from single and isolated adsorbates range over hard-wall approaches [88–90], sudden-approximation schemes [91], quantum wavepacket propagations [89, 92], the standard close-coupling gas phase approach [93], and atom–surface scattering formalisms [94]. In this subsection we are going to briefly analyse the same CO–Pt(111) system within the BB theory.

Large-momentum-transfer undulations were initially explained in a hard-wall model by the introduction of the so-called reflection symmetry interference (RSI) [88, 90]. Briefly, in such a model, the surface is represented as a mirror and the admolecule as a hemispherical boss from the mirror. The scattering amplitude can be then written as a sum of two contributions:

(a) a directly back-scattering term (involving only the adsorbate), f_a; and
(b) a term corresponding to the double reflection from both the hemisphere and the mirror surface, f_b.

To each of these two contributions, there are again two more contributions: one accounts for the predominantly wide-angle scattering from the illuminated face of the boss, f_{face}, and the other comes from the predominantly forward-scattering Fraunhofer diffraction, f_F. Theoretical studies by Yinnon *et al* [91] showed that not all of the oscillations observed could be attributed to Fraunhofer peaks. Rainbow effects due to the local corrugation caused by the defect were predicted from their classical trajectories calculations using a soft interaction potential. In a later work, Lemoine [93] corroborated the presence of rainbow peaks by numerically solving the time-dependent Schrödinger equation for the motion of the atomic scatterer.

A simple two-dimensional, soft-potential model, originally proposed by Yinnon *et al*, has been chosen for performing our quantum trajectories calculations. It consists of the sum of the interaction between He and the flat Pt(111) surface and the interaction between He and the spherically symmetric CO adsorbate:

$$V_{\text{He–CO/Pt(111)}}(\boldsymbol{r}) = V_{\text{He–Pt(111)}}(z) + V_{\text{He–CO}}(\boldsymbol{r} - \boldsymbol{r}_{\text{CO}}), \tag{69}$$

where $\boldsymbol{r}_{\text{CO}}$ and $\boldsymbol{r} = (x, z)$ give the position vectors of the CO centre of mass and of the He, respectively; z is the scattering coordinate perpendicular to the surface, and x is the coordinate parallel to the surface. The He–Pt(111) interaction is represented by a Morse function, like equation (66), with $D_s = 4.0$ meV, $\alpha = 0.6$ Bohr^{-1}, and $z_m = 2.3$ Bohr. In contrast, a Lennard-Jones function is chosen to describe the He–CO interaction with parameters $\epsilon = 2.37$ meV and $r_m = 3.5$ Å.
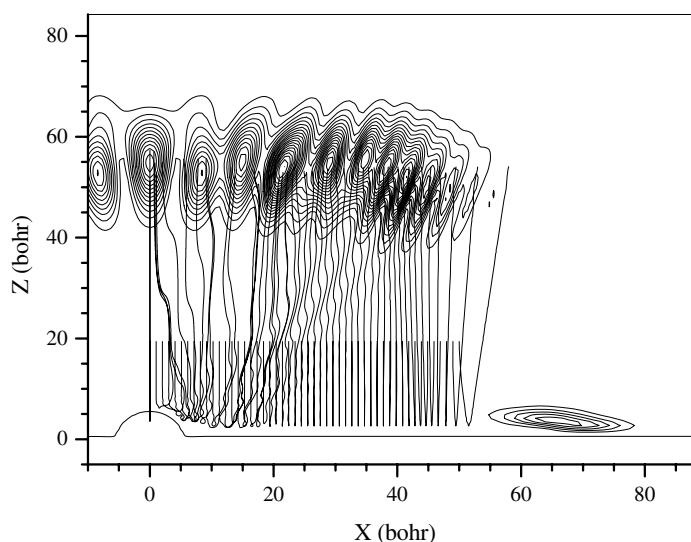
Figure 21. Bohmian trajectories corresponding to the case of figure 19 with $z_0 = \langle z \rangle_0 = 19.4$ Bohr.
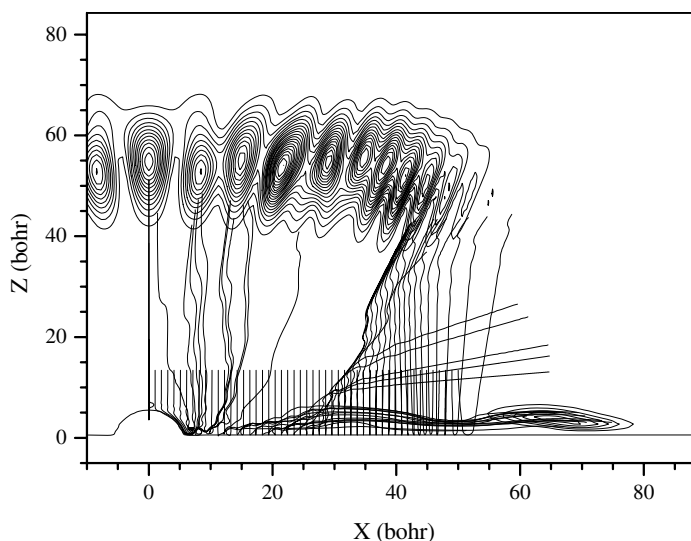
Figure 22. Bohmian trajectories corresponding to the case of figure 19 with $z_0 = 13.4$ Bohr.

The incoming plane wave has been considered to be a superposition of 250 Gaussian wavepackets, located along a distance of 100 Bohr (symmetrically distributed with respect to $x = 0$), as that given by equation (56). The values for the different components of the matrix $\underline{A}_0$ have been chosen such that their real parts are zero, and the imaginary parts (which give the initial spreading of the incoming packet) are taken considering that $\sigma_x \simeq 1.58$ Bohr and $\sigma_z = 5$ Bohr. Notice that in each length equal to σ_x, we can introduce approximately four Gaussian packets (the distance between two consecutive centres is 0.4 Bohr), which implies a very good overlapping among them. Moreover, this initial incoming wave has been centred at 19.4 Bohr, from the CO centre of mass in the simulation. The plane wave was

propagated for 5.5 ps and on a two-dimensional grid of size given by $n_x = 256$ and $n_z = 128$. In figure 19, the incoming (quasi-) plane wave at $t = 0$ ps (left), with incident energy of 10 meV and normal incidence, and the scattered wave at $t = 5.5$ ps (right) are both plotted. In figure 20, the corresponding final scattering distribution of the He atoms displayed is also in fairly good agreement with that shown in [92]. The first oscillations are assigned to Fraunhofer oscillations and the last ones to rainbow features.

Finally, in figures 21 and 22, quantum trajectories starting at $z_0 = 19.4$ and 13.4 Bohr, respectively, together with $|\Psi|^2$ at 5.5 ps, are shown. It is clearly seen how the quantum trajectories are following tracks of maximum probability density in both cases. An important difference between the two figures is that the set of quantum trajectories starting closest to the surface are contributing mainly to the border regions of the final wavepacket—in particular, to that remaining for a longer time along the surface. Furthermore, an incipient quantum vortex can be seen in the region near to the adsorbate. Several comments are in order. First, not all of the regions of the initial wavepacket contribute equally to the final diffracted intensity. Thanks to the quantum trajectories, we can divide the initial wavepacket into planes parallel to the x-axis and decide to what final lobe the wavepacket will be addressed. Second, the concept of RSI in this theoretical formalism is not necessary. Quantum trajectories are not straight lines around the interaction region; they can follow the boss profile of the adsorbate for a certain time; even some circular orbits (quantum vortices) are observed. In fluid mechanics language, a turbulent regime is obviously found around the adsorbate. And, third, the part of the final wavepacket adsorbed on the surface up to 5.5 ps could be responsible for a resonance phenomenon if another adsorbate were found along the surface. This is a well-known effect called defect-mediated-diffraction selective adsorption resonance [95] and predicted for adsorbates by Yinnon *et al*.

Acknowledgments

References

[1] Ballentine L E 1998 *Quantum Mechanics. A Modern Development* (Singapore: World Scientific)
[2] Feynman R P, Leighton R B and Sands M 1965 *The Feynman Lectures on Physics* vol 3 (Reading, MA: Addison-Wesley)
[3] Shull C G 1969 *Phys. Rev.* **179** 752
[4] Zeilinger A, Gähler R, Shull C G, Treimer W and Mampe W 1988 *Rev. Mod. Phys.* **60** 1067
[5] Schöllkopf W and Toennies J P 1994 *Science* **266** 1345
    Grisenti R E, Schöllkopf W, Toennies J P, Hegerfeldt G C and Köhler T 1999 *Phys. Rev. Lett.* **83** 1755
    Doak R B, Grisenti R E, Rehbein S, Schmahl G, Toennies J P and Wöll Ch 1999 *Phys. Rev. Lett.* **83** 4229
[6] Arndt M, Nairz O, Vos-Andreae J, Keller C, van der Zouw G and Zeilinger A 1999 *Nature* **401** 680
[7] Poelsema B and Comsa G 1989 *Scattering of Thermal Energy Atoms from Disordered Surfaces (Springer Tracts in Modern Physics vol 115)* (Berlin: Springer)
[8] Hulpke E 1992 (ed) *Helium Atom Scattering from Surfaces* (Berlin: Springer)
[9] Farias D and Rieder K H 1998 *Rep. Prog. Phys.* **61** 1575 and references therein
[10] Toennies J P 1991 *Surface Phonons (Springer Series in Surface Sciences vol 21)* ed W Kress and F W de Wette (Berlin: Springer) pp 111–66
[11] Gumhalter B 2001 *Phys. Rep.* **351** 1
[12] Stinnett J A, Madix R J and Tully J C 1996 *J. Chem. Phys.* **104** 3134
[13] Borondo F, Guantes R, Bowers J, Jaffé C and Miret-Artés S 1999 *Hamiltonian Systems with Three and More Degrees of Freedom* ed C Simó (Dordrecht: Kluwer) p 314
[14] Brivio G P and Grimley T B 1993 *Surf. Sci. Rep.* **17** 1

[15] D'Evelyn M P and Madix R J 1983 *Surf. Sci. Rep.* **3** 413
[16] Wolken G Jr 1973 *J. Chem. Phys.* **58** 3047
     Wolken G Jr 1973 *J. Chem. Phys.* **59** 1159
[17] Manolopoulos D E, Wyatt R E and Clary D C 1990 *J. Chem. Soc. Faraday Trans.* **86** 1641
[18] Miret-Artés S 1995 *Surf. Sci.* **339** 205
     Miret-Artés S 1996 *Surf. Sci.* **366** L681
[19] See for example:
     Tully J C 1980 *Annu. Rev. Phys. Chem.* **52** 933
     Adelman S A 1980 *Adv. Chem. Phys.* **44** 143
     Barker J A and Auerbach D J 1985 *Surf. Sci. Rep.* **4** 1
     Gerber R B 1987 *Chem. Rev.* **87** 29
[20] Kleyn A W and Horn T C M 1991 *Phys. Rep.* **199** 193
[21] McClure J D 1969 *J. Chem. Phys.* **51** 9687
     McClure J D 1970 *J. Chem. Phys.* **52** 2712
     McClure J D 1972 *J. Chem. Phys.* **57** 2810
     McClure J D 1972 *J. Chem. Phys.* **57** 2823
[22] Steele W A 1973 *Surf. Sci.* **38** 1
     Jewsbury P 1975 *Surf. Sci.* **52** 325
     Klein J R and Cole M W 1979 *Surf. Sci.* **79** 269
     Klein J R and Cole M W 1979 *Surf. Sci.* **81** L319
     Baker J A, Dion D R and Merrill 1980 *Surf. Sci.* **95** 15
     Hubbard L M and Miller W H 1983 *J. Chem. Phys.* **78** 1801
     Moiseyev N, Maniv T, Elber R and Gerber R B 1985 *Mol. Phys.* **55** 1369
[23] McCann K J and Celli V 1974 *Surf. Sci.* **61** 954
[24] Sathyamurthy N and Toennies J P 1988 *Chem. Phys. Lett.* **143** 323
     Kumar S and Sathyamurthy N 1990 *Chem. Phys. Lett.* **175** 616
     Thareja S and Sathyamurthy N 1990 *Surf. Sci.* **237** 266
     Polanyi J C and Wolf R J 1982 *Ber. Bunsenges. Phys. Chem.* **86** 356
[25] Lennard-Jones J E and Devonshire A F 1936 *Nature* **137** 1069
[26] Gorse D, Salanon B, Fabre F, Kara A, Perreau J, Armand G and Lapujoulade J 1984 *Surf. Sci.* **47** 611
     Henández M, Miret-Artés S, Villarreal P and Delgado-Barrio G 1992 *Surf. Sci.* **274** 21
     Henández M, Miret-Artés S, Villarreal P and Delgado-Barrio G 1993 *Surf. Sci.* **290** L693
[27] Guantes R, Borondo F and Miret-Artés S 1997 *Phys. Rev.* E **56** 378
[28] Eckhardt B 1988 *Physica* D **33** 89
[29] Borondo F, Jaffé C and Miret-Artés S 1994 *Surf. Sci.* **317** 211
[30] Garibaldi U, Levi A C, Spadacini R and Tommei G E 1975 *Surf. Sci.* **48** 649
[31] Berry M V 1975 *J. Phys. A: Math. Gen.* **8** 566
[32] Doll J D 1974 *J. Chem. Phys.* **61** 954
     Masel R I, Merrill R P and Miller W H 1976 *J. Chem. Phys.* **64** 45
     Guantes R, Borondo F, Jaffé C and Miret-Artés S 1996 *Phys. Rev.* B **53** 14 117
[33] An excellent monograph on the causal interpretation of quantum mechanics can be found in:
     Holland P R 1993 *The Quantum Theory of Motion* (Cambridge: Cambridge University Press)
[34] Madelung E 1926 *Z. Phys.* **40** 332
[35] de Broglie L 1925 *Ann. Phys., Paris* **3** 22
     de Broglie L 1925 Recherches sur la théorie des quanta *Doctoral Thesis* Universitée de Paris
[36] Bohm D 1952 *Phys. Rev.* **85** 166
     Bohm D 1952 *Phys. Rev.* **85** 194
[37] Cushing J T, Fine A and Goldstein S 1996 *Bohmian Mechanics: an Appraisal* (Boston, MA: Kluwer)
[38] Bohm D, Hiley B J and Kaloyeru P N 1987 *Phys. Rep.* **144** 321
[39] Hirschfelder J O, Christoph A C and Palke W E 1975 *J. Chem. Phys.* **61** 5435
[40] Dewdney C and Hiley B J 1982 *Found. Phys.* **12** 27
[41] Philippidis C, Dewdney C and Hiley B J 1979 *Nuovo Cimento* B **52** 15
[42] Dewdney C, Holland P R, Kyprianidis A and Vigier J P 1988 *Nature* **336** 536
[43] Brown H R, Sjöqvist E and Bacciagaluppi G 1999 *Phys. Lett.* A **251** 229
[44] Parmenter R H and Valentine R W 1995 *Phys. Lett.* A **201** 1
     Parmenter R H and Valentine R W 1997 *Phys. Lett.* A **227** 5
[45] Konkel S and Makowski A J 1998 *Phys. Lett.* A **238** 95
[46] Sales-Mayor F, Askar A and Rabitz H 1999 *J. Chem. Phys.* **111** 2423

[47] Lopreore C L and Wyatt R E 1999 *Phys. Rev. Lett.* **82** 5190
     Wyatt R E 1999 *Chem. Phys. Lett.* **313** 189
     Lopreore C L and Wyatt R E 2000 *Chem. Phys. Lett.* **325** 73
[48] Burant J C and Tully J C 2000 *J. Chem. Phys.* **112** 6097
[49] Sanz A S, Borondo F and Miret-Artés S 2000 *Phys. Rev.* B **61** 7743
[50] Sanz A S, Borondo F and Miret-Artés S 2001 *Europhys. Lett.* **55** 303
[51] Gindensperger E, Meier C and Beswick J A 2000 *J. Chem. Phys.* **113** 9369
[52] Gindensperger E, Meier C and Beswick J A 2002 *J. Chem. Phys.* **116** 8
     Gindensperger E, Meier C, Beswick J A and Heitz M C 2002 *J. Chem. Phys.* at press
[53] Wheeler J A and Zurek W H (ed) 1983 *Quantum Theory of Measurement* (Princeton, NJ: Princeton University
     Press)
[54] Ballentine L E 1970 *Rev. Mod. Phys.* **42** 358
[55] Bohm D 1953 *Phys. Rev.* **89** 458
[56] Bell J S 1966 *Rev. Mod. Phys.* **38** 447
[57] Landau L D and Lifshitz E M 1959 *Fluid Mechanics* (Oxford: Pergamon)
[58] Bialynicki-Birula I, Cieplak M and Kaminski J 1992 *Theory of Quanta* (Oxford: Oxford University Press) ch 9
[59] Skodje R T, Rohrs H W and VanBuskirk J 1989 *Phys. Rev.* A **40** 2894
[60] London F 1945 *Rev. Mod. Phys.* **17** 310
[61] Fetter A L and Svidzinsky A A 2001 *J. Phys.: Condens. Matter* **13** R135
[62] Dirac P A M 1931 *Proc. R. Soc.* A **133** 60
[63] Riess J 1970 *Phys. Rev.* D **2** 647
[64] Hirschfelder J O, Goebel C J and Bruch L W 1974 *J. Chem. Phys.* **61** 5456
[65] Wu H and Sprung D W L 1994 *Phys. Rev.* A **49** 4305
[66] Bialynicki-Birula I and Bialynicka-Birula Z 1971 *Phys. Rev.* D **3** 2410
[67] Aharonov Y and Bohm D 1959 *Phys. Rev.* **115** 485
[68] Liboff R L 1984 *Phys. Today* **37** 50
[69] Berry M V 1989 *Phys. Scr.* **40** 335
[70] Weiner J H and Partom Y 1969 *Phys. Rev.* **187** 1134
[71] Weiner J H and Askar A 1971 *J. Chem. Phys.* **54** 3534
[72] Dewdney C and Malik Z 1993 *Phys. Rev.* A **48** 3513
[73] Parmenter R H and Valentine R W 1995 *Phys. Lett.* A **201** 1
[74] Heller E J 1975 *J. Chem. Phys.* **62** 1544
[75] Feit M D, Fleck J A and Steiger A 1982 *J. Comput. Phys.* **47** 412
[76] Kosloff D and Kosloff R 1983 *J. Comput. Phys.* **52** 35
[77] Tal-Ezer H and Kosloff R 1984 *J. Chem. Phys.* **81** 3967
[78] Press W H, Flannery B P, Teukolsky S A and Vetterling W T 1986 *Numerical Recipes: the Art of Scientific
     Computing* (Cambridge: Cambridge University Press) ch 12
[79] Oriols X, Martín F and Suñé J 1996 *Phys. Rev.* A **54** 2594
[80] Drolshagen G and Heller E J 1983 *J. Chem. Phys.* **79** 2072
[81] Goldberg A, Schey H M and Schwartz J L 1967 *Am. J. Phys.* **35** 177
[82] Kosloff D and Kosloff R 1983 *J. Chem. Phys.* **79** 1823
[83] Leforestier C *et al* 1991 *J. Comput. Phys.* **94** 59
[84] Elmore W C and Heald M A 1985 *Physics of Waves* (New York: Dover) ch 10
[85] Giulini D, Kiefer C, Kupsch J, Stamatescu I O and Zeh H D 1996 *Decoherence and the Appearance of a Classical
     World in Quantum Theory* (Berlin: Springer)
[86] Miret-Artés S, Margalef-Roig J, Guantes R, Borondo F and Jaffé C 1996 *Phys. Rev.* B **54** 10 397
     Guantes R, Borondo F, Jaffé C and Miret-Artés S 1995 *Surf. Sci.* **338** L863
[87] Bertet P, Osnaghi S, Rauschenbeutel A, Nogues G, Auffeves A, Brune M, Raimond J M and Haroche S 2001
     Nature **411** 166
[88] Lahee A M, Manson J R, Toennies J P and Wöll Ch 1986 *Phys. Rev. Lett.* **57** 471
     Lahee A M, Manson J R, Toennies J P and Wöll Ch 1987 *J. Chem. Phys.* **86** 7194
[89] Drolshagen G and Vollmer R 1987 *J. Chem. Phys.* **87** 4948
[90] Graham A P, Hofman F, Toennies J P and Manson J R 1996 *J. Chem. Phys.* **105** 2093
[91] Yinnon A T, Kosloff R and Gerber R B 1988 *J. Chem. Phys.* **88** 7209
[92] Carré M and Lemoine D 1994 *J. Chem. Phys.* **101** 5305
[93] Lemoine D 1998 *Phys. Rev. Lett.* **81** 461
[94] Choi B H, Graham A P, Tang K T and Toennies J P 2000 *J. Chem. Phys.* **112** 10 538
[95] Glebov A, Manson J R, Skofronick and Toennies J P 1997 *Phys. Rev. Lett.* **78** 1508